Featured in Physics

Joint analysis of Dark Energy Survey Year 3 data and CMB lensing from SPT and Planck. I. Construction of CMB lensing maps and modeling choices

Y. Omorio, 1.2.3.4 E. J.Baxter, C. Chang, O. Friedrich, A. Alarcon, O. Alves, A. Amon, F. Andrade-Oliveira, K. Bechtol, M. R. Becker, G. M. Bernstein, J. Blazek, 12.13 L. E. Bleem, 14.2 H. Camacho, A. Campos, A. Campos,

(DES and SPT Collaborations)

```
Departmentof Astronomy and Astrophysicklniversity of Chicago, Chicago, Illinois 60637, USA
   <sup>2</sup>Kavli Institute for CosmologicaPhysics,University of Chicago, Chicago, Illinois 60637, USA
<sup>3</sup>Department ofPhysics,Stanford University,382 Via Pueblo Mall,Stanford,California 94305,USA
    <sup>4</sup>Kavli Institute for Particle Astrophysics and Cosmologty, O. Box 2450,Stanford University,
                                  Stanford, California 94305, USA
<sup>5</sup>Institute for AstronomyUniversity of Hawai'i, 2680 Woodlawn DriveHonolulu, Hawaii 96822, USA
                      <sup>6</sup>Kavli Institute for CosmologyUniversity of Cambridge,
                      Madingley Road Cambridge CB3 0HA United Kingdom
        Argonne NationalLaboratory, 9700 South Cass Avenubemont, Illinois 60439, USA
         <sup>8</sup>Departmentof Physics,University of Michigan, Ann Arbor, Michigan 48109,USA
         <sup>9</sup>Laboratório Interinstitucionalde e-Astronomia - LIneARua Gal. Jo≆ Cristino 77,
                                Rio de Janeiro, RJ 20921-400 Brazil
           <sup>10</sup>Physics Department 320 Chamberlin Hall, University of Wisconsin-Madison,
                   1150 University Avenue MadisoMyisconsin 53706-1390JSA
                <sup>11</sup>Department of Physics and AstronomyUniversity of Pennsylvania,
                               Philadelphia, Pennsylvania 19104USA
        <sup>12</sup>Department of Physics, Northeastern University Boston, Massachusetts 02115, SA
          <sup>13</sup>Laboratory of AstrophysicsÉcole Polytechnique €dérale de Lausanne (EPFL),
                        Observatoire de Sauvern 1290 Versoix, Switzerland
                   <sup>14</sup>High-Energy Physics DivisionArgonne NationalLaboratory,
                      9700 South Cass Avenue Argonne, Illinois 60439, USA
     <sup>15</sup>Instituto de Física TeóricaUniversidade EstaduaPaulista,São Paulo 01140-070₿razil
     <sup>16</sup>Department of Physics, Carnegie Mellon University Pittsburgh, Pennsylvania 15312 JSA
              <sup>7</sup>Instituto de Astrofisica de Canarias -38205 La Laguna, Tenerife, Spain
    <sup>18</sup>Universidad de La LagunaDepartamento AstrofísicÆ-38206 La Laguna,Tenerife,Spain
         Center for AstrophysicaSurveysNational Center for Supercomputing Applications,
                        1205 WestClark Street, Urbana, Illinois 61801, USA
```

```
<sup>20</sup>Department of Astronomy, University of Illinois at Urbana-Champaign,
                        1002 W. Green Street Urbana, Illinois 61801, USA
           <sup>21</sup>Physics Department/Villiam Jewell College_Liberty, Missouri 64068, USA
          <sup>22</sup>Department of Physics Duke University Durham North Carolina 27708, USA
      <sup>23</sup>California Institute of Technology, 1200 East California Blvd, MC 249-17, Pasadena,
                                      California 91125, USA
<sup>24</sup>Jodrell Bank Center for Astrophysic School of Physics and Astronom University of Manchester,
                       Oxford Road, Manchester M13 9PLUnited Kingdom
            <sup>25</sup>Institut d'Estudis Espacials de Catalunya (IEEQ)8034 BarcelonaSpain
         <sup>26</sup>Institute of Space Sciences (ICESIC), Campus UAB, Carrer de Can Magrans,
                                    s/n, 08193 BarcelonaSpain
  <sup>27</sup>Lawrence Berkeley Nationalaboratory, 1 Cyclotron Road, Berkeley, California 94720, USA
         <sup>28</sup>NSF AI Planning Institute for Physics offhe Future, Carnegie Mellon University,
                               Pittsburgh, Pennsylvania 15213 JSA
      <sup>29</sup>Fermi National Accelerator Laboratory P. O. Box 500, Batavia, Illinois 60510, USA
              <sup>30</sup>Department ofAstronomy/Steward ObservatorUniversity of Arizona,
                   933 North Cherry AvenueTucson, Arizona 85721-0065USA
                  <sup>31</sup>Jet Propulsion Laboratory,California Institute of Technology,
                      4800 Oak Grove Dr., Pasadena California 91109, USA
               <sup>32</sup>Departmentof Physics and AstronomyUniversity College London,
                        Gower Street London WC1E 6BT United Kingdom
          <sup>33</sup>Center for Cosmology and Astro-Particle Physion, Ohio State University,
                                   Columbus, Ohio 43210, USA
         <sup>34</sup>Departmentof Physics,The Ohio State UniversityColumbus,Ohio 43210,USA
          35Santa Cruz Institute for Particle PhysicSanta Cruz, California 95064, USA
   <sup>36</sup>Departmentof Astronomy,University of California, Berkeley,501 CampbellHall, Berkeley,
                                      California 94720, USA
  <sup>37</sup>Institut de Física d'Altes Energies (IFAE)The Barcelona Institute o6cience and Technology,
                        Campus UAB 08193 Bellaterra (Barcelona) Spain
           38Excellence Cluster OriginsBoltzmannstrasse 23,5748 Garching,Germany
 <sup>39</sup>Faculty of Physics,Ludwig-Maximilians-UniversitätScheinerstrasse 181679 Munich,Germany
       <sup>10</sup>Departmentof Physics, University of Oxford, Denys Wilkinson Building Keble Road,
                                Oxford OX1 3RH, United Kingdom
    <sup>41</sup>Schoolof Physics and AstronomyCardiff University, Cardiff CF24 3AA, United Kingdom
            <sup>2</sup>Department of Physics, University of Arizona, Tucson, Arizona 85721, USA
         <sup>43</sup>Department ofPhysics and AstronomyPevensey BuildingUniversity ofSussex,
                               Brighton BN1 9QH, United Kingdom
     <sup>44</sup>Institute for AstronomyUniversity ofEdinburgh,Edinburgh EH9 3HJ,United Kingdom
  <sup>45</sup>Instituto de Astrofísica e Ciências do Espaç<del>o</del>aculdade de Ciências Jniversidade de Lisboa,
                                    1769-016 Lisboa Portugal
         <sup>46</sup>Perimeter Institute for Theoretica Physics, 31 Caroline Street North, Waterloo,
                                     Ontario N2L 2Y5, Canada
     <sup>47</sup>Departmentof Applied Mathematics and Theoretic hysics, University of Cambridge,
                              Cambridge CB3 0WAUnited Kingdom
           <sup>48</sup>SLAC NationalAccelerator Laboratory, Menlo Park, California 94025, USA
             <sup>49</sup>Instituto de Física Gleb Wataghir Universidade Estadual de Campinas,
                              13083-859 CampinasŞão Paulo, Brazil
          <sup>50</sup>Kavli Institute for the Physics and Mathematics bfe Universe (WPI)UTIAS,
                    The University ofTokyo, Kashiwa, Chiba 277-8583, Japan
      <sup>51</sup>ICTP South American Institute for Fundamentalesearch Instituto de Física Teórica,
                   Universidade EstaduaPaulista, São Paulo 01140-070Brazil
       <sup>52</sup>Centro de Investigaciones Enæticas, Medioambientales y Tecnológicas (CIEMAT),
                                       Madrid 28040, Spain
            53Brookhaven NationaLaboratory, Bldg 510, Upton, New York 11973,USA
 <sup>54</sup>Départementle Physique Teórique and Center for Astroparticle Physicklniversité de Gereve,
                      24 quai ErnestAnsermet,CH-1211 GenevaSwitzerland
<sup>55</sup>Max Planck Institute for ExtraterrestriaPhysics,Giessenbachstrass&5748 Garching,Germany
     <sup>56</sup>Universitäts-Sternwarte, akultät für Physik, Ludwig-Maximilians Universitä München,
                           Scheinerstrasse 181679 München Germany
```

```
<sup>57</sup>Cerro Tololo Inter-American Observator)NSF's NationalOptical-Infrared Astronomy Research
                             Laboratory, Casilla 603, La Serena, Chile
                 <sup>58</sup>Institute ofCosmology and GravitationUniversity ofPortsmouth,
                              Portsmouth PO1 3FXUnited Kingdom
           <sup>59</sup>Institut d'Astrophysique de ParisCNRS,UMR 7095,F-75014 Paris,France
       60 Institut d'Astrophysique de ParisSorbonne Université, UPMC Université Paris 06,
                                 UMR 7095, F-75014 Paris, France
           <sup>61</sup>University ObservatoryFaculty of Physics,Ludwig-Maximilians-Universität,
                             Scheinerstrasse 181679 Munich, Germany
<sup>62</sup>Enrico Fermi Institute, University of Chicago, 5640 South Ellis Avenue, Chicago, Illinois 60637, USA
<sup>63</sup>Department of Physics, University of Chicago, 5640 South Ellis Avenue, Chicago, Illinois 60637, USA
        <sup>64</sup>Department of Physics and Astronomy, he University of Western Ontario London,
                                     Ontario N6A 3K7, Canada
           <sup>65</sup>Institute for Earth and Space Exploration, he University of Western Ontario,
                                London, Ontario N6A 3K7, Canada
<sup>66</sup>Astronomy Unit,Department ofPhysics,University ofTrieste,via Tiepolo 11,I-34131 Trieste,Italy
       <sup>67</sup>INAF-Osservatorio Astronomico dirieste, via G. B. Tiepolo 11,I-34143 Trieste, Italy
       <sup>68</sup>Institute for FundamentaPhysics of the Universe, Via Beirut 2, 34014 Trieste Italy
<sup>69</sup>Observatório NacionalRua Gal. José Cristino 77, Rio de Janeiro Rio de Janeiro 20921-40 Brazil
                  <sup>70</sup>Departmentof Astronomy & AstrophysicsUniversity of Toronto,
                       50 St George St, Toronto, Ontario M5S 3H4, Canada
   <sup>71</sup>Hamburger SternwarteUniversitätHamburg,Gojenbergsweg 11221029 Hamburg,Germany
     High Energy Accelerator Research Organization (KEKT)sukuba, Ibaraki 305-0801, Japan
          Department of Physics, University of California, Berkeley, California 94720, USA
               ⁴Departmentof Physics,IIT Hyderabad,Kandi, Telangana 502285lındia
               <sup>75</sup>Departmentof Physics and McGillSpace InstituteMcGill University,
                     3600 Rue UniversityMontreal, Quebec H3A 2T8Canada
 <sup>76</sup>Canadian Institute for Advanced Research FAR Program in Gravity and the Extreme Universe,
                                Toronto, Ontario M5G 1Z8, Canada
           <sup>77</sup>Departmentof Astrophysicaland Planetary Sciences Iniversity of Colorado,
                                   Boulder, Colorado 80309, USA
                      <sup>78</sup>Institute ofTheoreticalAstrophysicsUniversity ofOslo,
                         P. O. Box 1029 Blindern, NO-0315 Oslo, Norway
  <sup>79</sup>Instituto de Fisica Teorica UAM/CSIQJniversidad Autonoma de Madriq28049 Madrid, Spain
     80European Southern Observatorkarl-Schwarzschild-Straße 25,5748 Garching,Germany
                 <sup>81</sup>Institute of Astronomy, University of Cambridge, Madingley Road,
                               Cambridge CB3 0HAUnited Kingdom
          82Departmentof Physics, University of Colorado, Boulder, Colorado 80309, USA
<sup>83</sup>School of Mathematics and Physidsniversity of QueenslandBrisbane, Queensland 4072Australia
                <sup>84</sup>Departmentof Physics University of Illinois at Urbana-Champaign.
                        1110 WestGreen StreetUrbana, Illinois 61801, USA
           85University of Chicago, 5640 South Ellis Avenu@hicago, Illinois 60637, USA
                         86Center for AstrophysicsHarvard & Smithsonian,
                     60 Garden StreetCambridge, Massachusetts 0213&ISA
<sup>87</sup>Departmentof Physics, University of California, One Shields Avenu@avis, California 95616, USA
<sup>88</sup>Australian Astronomical Optics, Macquarie University, North Ryde, New South Wales 2113, Australia
             <sup>89</sup>Lowell Observatory,1400 Mars Hill Road,Flagstaff,Arizona 86001,USA
       <sup>90</sup>Departamento de Física Matemáticanstituto de Física, Universidade de São Paulo,
                        CP 66318, São Paulo, São Paulo 05314-970 Prazil
                    <sup>91</sup>Departmentof AstrophysicalSciencesPrinceton University,
                          Peyton Hall, Princeton, New Jersey 08544USA
           92 Institució Catalana de Recerca i Estudis Avança Es 08010 Barcelona Spain
           93Excellence Cluster Universeoltzmannstrasse 2,5748 Garching,Germany
      <sup>94</sup>Universitäts-Sternwarte, akultät für Physik, Ludwig-Maximilians Universitä München,
                            Scheinerstrasse 181679 München Germany
  <sup>95</sup>Schoolof Physics and AstronomyUniversity ofMinnesota,116 Church StreeSE Minneapolis,
                                       Minnesota 55455USA
          96Schoolof Physics, University of Melbourne, Parkville, Victoria 3010, Australia
      <sup>97</sup>Departmentof Physics,Case Western Reserve Universi©leveland,Ohio 44106,USA
   <sup>98</sup>Liberal Arts DepartmentSchoolof the Art Institute of Chicago, Chicago, Illinois 60603, USA
```

99School of Physics and Astronomy, University of Southampton, Southampton SO17 1BJ, United Kingdom ¹⁰⁰Harvard-Smithsonian Center for Astrophysi**®**0 Garden StreetCambridge, Massachusetts 0213&ISA ¹⁰¹Computer Science and Mathematics Divisi**ŵ**ak Ridge NationaLaboratory, Oak Ridge, Tennessee 3783 USA

(Received 31 March 2022accepted 12 December 202@ublished 31 January 2023)

Joint analyses of cross-correlations between measurements of galaxy positizations lensing and lensing of the cosmic microwave background (CMB) offer powerful constraints on the large-scale structure of the Universe. In a forthcoming analysis, we will present cosmological constraints from the analysis of such cross-correlations measured using Year 3 data from the Dark Energy Survey (DES), and CMB data from the South Pole Telescope (SPT) and Planck. Here we present two key ingredients of this analysis: (1) an improved CMB lensing map in the SPT-SZ survey footprint and (2) the analysis methodology that will be used to extractosmologicalinformation from the cross-correlation measurements lative to previous lensing maps made from the same CMB observations have implemented techniques to remove contamination from the thermal Sunyaev Zel'dovich effect, enabling the extraction of cosmological information from smaller angular scales of the cross-correlation measurements than in previous analyses with DES Year 1 data. We describe our model for the cross-correlations between these maps and DES data, and validate our modeling choices to demonstrate the robustness of our analysisthen forecasthe expected cosmological constraints from the galaxy survey-CMB lensing auto and cross-correlations. We find that the galaxy-CMR lensing and galaxy shear-CMB lensing correlations will on their own provide a constraint on §1/4 σ_8 Ω_m =0.3 at the few percent level, providing a powerful consistency check for the DES-only constraints. We explore scenarios where external priors on shear calibration are removed, finding that the joint analysis of CMB lensing cross-correlations can provide constraints on the shear calibration amplitude at the 5% to 10% level.

DOI: 10.1103/PhysRevD.107.023529

I. INTRODUCTION

Cross-correlations of alaxy surveys with overlapping measurements of cosmic microwave background (CMB) lensing offer a powerful way to probe the large-scale structure (LSS) of the UniverseGalaxy imaging surveys use measurements of the positions of galaxies and of the survey of roughly 5; 000 deg, with cosmological congravitationalshearing of galaxy images to trace the LSS. For current imaging surveys [1–3], these measurements typically become less sensitive at z ≥ 1, as galaxies becore evides roughly 2; 500 degof high-sensitivity and highmore difficult to detect and characterize at higher redshiftsingular resolution CMB data that overlaps with DES Gravitational lensing of the CMB probes the LSS across abservationsAt the same time. Planck provides maps of broad range of redshift, and is most sensitive to structure AB lensing that overlap with the full 5; 000 ded DES z ~ 2. Cross-correlationsof galaxy surveys with CMB lensing can exploit this sensitivity to achieve tighter constraints on the high-redshift Universe than with galaxy surveys alone [e.g., [4–11]]. CMB lensing also offers a probe of LSS that shares (almost) no sources of systema@MB lensing to constrain cosmology [e.g., [4-6,17]]. error with measurements from galaxy surveys. For instance, unlike galaxies used to measure gravitational lensing, the redshift of the CMB is precisely known. CMB lensing is also not impacted by effects such as intrinsic alignments. Consequently cross-correlations of galaxy and CMB lensing are expected to offer especially robust probes of LSS [e.g., [12,13]]. This is an exciting prospectsince control of systematic uncertainties in LSS surveys has become increasingly importants statistical uncertainties have continued to decrease.

The Dark Energy Survey [DES, [1]] and the South Pole Telescope [SPT[14]] provide state-of-the-articleary and CMB datasets, respectively, that overlap across a large area on the sky, and are therefore very well suited to crosscorrelation analyses. DES has recently completed a six year straints from the first three years (Y3) of data presented in [15]. The SPT-SZ survey was completed in 2011, and survey region albeit with higher noise and lower angular resolution than SPT-SZ [16].

Several recent analyses have used cross-correlations between earlierDES data and SPT-SZ measurements of In particular, [17] presented a joint analysis of crosscorrelations between firstyear (Y1) data from DES and CMB lensing measurements from SPT-SZ and Planck, using these correlations to constrain cosmological parameters, and to test for consistency between the galaxy survey and CMB lensing measurements. In that work, we analyzed six two-point functions between the galaxy density, galaxy lensing, and CMB lensing fields; we refer to this combination as 6 × 2pt. When leaving out the CMB lensing autocorrelationwe refer to the remaining combination of

probes as 5 × 2pt; the combination of two-point functions including our modeling and validation for the covariance 3 × 2pt. A challenge for the 5 × 2pt analysis presented tion prevented us from using the two-point function measurements asmall scales, resulting in a significant reduction in signal-to-noise ratio 19.9 to 9.9 and 10.8 to 6.8 for the galaxy-CMB lensing and shear-CMB lensing correlations respectively [5,6].

will be applied to the forthcoming analysis of crosscorrelations between Yeaß data from DES and CMB lensing maps from SPT-SZ and Planck. The CMB lensing map presented here is constructed in a way threemoves contamination from the tSZ, enabling a much larger fraction of the measured signal (and in particular the information at small angular scales) to be used to constrain cience Foundation Amundsen-Scotouth Pole station maps to show that they are free from significant biases.

The modeling framework thatwe presentis similar to that developed in [18], but incorporates several improvements. These include new models for intrinsic alignmentswe primarily focus on the 150 GHz data since its noise the impact of lensing magnification of the galaxy sample, level (\sim 18 μ K-arcmin) is lower than that of the 90 and modeling of nonlinear galaxy bias, and the use of lensing 220 GHz data (40 and 70 µK-arcminrespectively) [22]. ratios. We additionally describe the estimation of a covari-We start with the same data products as in [20] and ance matrix for the cross-correlation measurementand perform detailed validation of this estimate. Finally, we determine a sebf analysis choicesthat when applied to simulated data designed to replicate the real DES, SPT-SZ-construction procedure, since the tSZ-nulling method and Planck data, yield robust and unbiased constraints onwill eliminate the tSZ bias. The nulling procedure is cosmological models. The methodology developed here will be applied to data in a companion paper.

The highest signal-to-noise measurement the CMB lensing power spectrum to date is from the full-sky Planck mission [16]. Therefore, as in [17], we plan to present joint European Space agencywith the goal of making clean sented here. As we demonstrate below, since Planck covers from 30 to 857 GHz [23,24]. We rely on two trum measurements with the 5 × 2ptmeasurements prethe full sky and since the CMB lensing power spectrum is different temperature maps from Planck: primarily sensitive to higher redshifts than the 5 × 2pt combination, covariance between the two is negligible. We therefore consider the CMB lensing auto-spectrum as an external probe, and focus the methodological developments in this paper entirely on $5 \times 2pt$.

The paper is organized as follows. In Sec. II, we present the methodology used to construct the CMB lensing map from SPT and Planck data, as well as tests of these maps. We quantify the noise level in the maps, a key ingredient for determining the covariance of he cross-correlation measurements.In Sec. III we present our models for the correlations between these maps and DES galaxies and shears.In Sec. IV we describe our procedure for fitting the theoretical models to the two-point measurements,

between galaxy density and galaxy lensing is referred to anatrix. In Sec. V, we describe our procedure for selecting parts of the full data vector (i.e.the correlation measurein [17] was contamination of the CMB lensing maps by thements) for which we are sufficiently certain of the accuracy thermal Sunyaev-Zel'dovich (tSZ) effect. This contamina-of our model that we can use the measurements to constrain cosmological parameters. We present forecasts for cosmological constraints in SecVI. We conclude in SecVII.

II. tSZ-FREE CMB LENSING MAP

We begin by describing the data and methodology used In this work, we present an updated CMB lensing map as generate a CMB lensing map from SPT-SZ and Planck well as the modeling framework and analysis choices thatdata that is not biased by contamination from the tSZ effect.

A. Data

1. SPT-SZ temperature map

The SPT is a millimeter/submillimeter telescope with a 10 m aperture that is located at the National cosmology. We apply several tests to the new CMB lensing Antarctica. The SPT data used in this analysis is the same as used in [19-21], namely data from the 2500 deapT-SZ survey, which was conducted between 2008 and 2011. While the SPT-SZ camera had three frequency channels, reprocess the data to optimize for cross-correlation analyses. In particular, we reduce the number of masked regions around clusters before performing the lensing described in Sec.II D 2.

2. Planck data

maps of the CMB by observing the sky at nine frequencies

(i) Planck 143 GHz temperature mapBy combining the Planck data and SPT-SZ data overthe same footprint, we can improve signal-to-noise by recovering the modes that are removed in the SPT-SZ data due to filtering. To this end, we use the Planck 143 GHz full mission temperature map from the 2018 data release [25]. Additionally, we use the 300 full focal plane (FFP10) full mission noise

¹In [20], clusters detected with S/N greater than 5 in [22] were masked. In this study, we only mask clusters detected above S/N 10 in the temperaturemap before performing the lensing reconstruction.

The maps are publicly available from the Planck Legacy Archive: https://pla.esac.esa.int.

realizations for the purposes of computing the Planckower spectra. For the Poisson term, we place detected noise power. We describe the process of combining oint sources with their measured fluxes at their observed the SPT-SZ 150 GHz and Planck 143 GHz temper-locations.

ature data to improve signal-to-noise in Sec. II C. Planck SMICA tSZ-nulled (SMICAnoSZ)temperature map. Our reconstruction of the CMB lensing field from the CMB temperature data relies on the quadratic estimator[26], which estimates the lensing field using two (differently filtered) temperwas used for both legs.

In this study, we replace one of the legs with a lower-resolution and higher-noiseaut tSZ-cleaned temperature map generated from Planck daspecifically, we use Planck maps generated with the spectralmatching independentomponentanalysis (SMICA) algorithm [27,28]. SMICA takes the linear combinations of all three LFI and six HFI Planck frequency channels from 30 to 857 GHz [29] to produce the minimum-variance map ofhe CMB. The tSZ-free variant of this map, SMICAnoSZ, exploits the known frequency dependence of the the cosmic infrared background (CIB).3 Similar approacheshave been used to make tSZ-nulled CMB maps in other studies [31,32]. This temperature map is also the input for the SMICAnoSZ variant of the lensing map released by the Planck collaboration.

B. CMB simulations

quantities such as the response function, mean-field bias, at combining multiple frequency channels given the noise bias terms thatare used to produce normalized and signal-to-noise of our data, the data, the data when constructdebiased CMB lensing maps and CMB lensing auto-specing the lensing maps, and the smoothing that we apply to [16,20,33,34]. We begin by generating unlensed CMB N_{side} 1/4 8192, and also Gaussian realizations of the lensing negligible [40]. The tSZ component is simply removed using the LENSPIX package [36].

(i.e., non-CMB) sources of emission. We split these contributions into Gaussian and Poisson components. For the Gaussian component, we largely follow the simulation pipeline that was used in [20]: we take the best-fit model power spectrum of thermaSZ, kinematic SZ, cosmic infrared background (CIB) and radio sources from [37] and generate Gaussian realizations from those tions are not sufficient to asses biases coming from high-order

We generate 150 full-sky realizations of lensed CMB and Gaussian secondary realizations, d extracttwo patches at the opposite hemispheres. After extracting two SPT-SZsized patches from each realization—for total of 300 simulations of the SPT-SZ survey—we add clusters detected above 5σ in [22] and pointsources with fluxes ature maps, or "legs." In [20], the minimum-variance between 6.4 and 50 mJy in 150 GHz [38] and place them at combination of SPT 150 GHz and Planck 143 GHz their observed locations. This ensures that these sources are at the same locations in all of the realizations, which is important for computing the mean-field bias after reconstructing the lensing map.

From the sum of the simulated lensed CMB and foreground maps, we generate mock SPT-SZ and Planck maps. For SPT-SZ, we pass the extracted maps through a mockobserving pipeline. As described in [20,21], we compare the outputs of the 300 realizations from the mock observations with the input maps to compute the filter transfer function. We then add noise realizations obtained using the halfdifference techniquewhere half of the observations are multiplied with a minus sign, such that when the sum of all tSZ signal to remove the tSZ signal, in exchange for the observations are taken, the sky signal is nulled and noise a slight increase in the noise and potential bias from left. For Planck 143 GHz mocks, we simply convolve the input sky maps with the 143 GHz channel beamnd add the noise realizations from the FFP10 simulations.

Generating simulated maps corresponding to the

SMICAnoSZ maps is somewhatmore involved because

these use data from nine frequency channe Generating

foreground models across these bands would require detailed knowledge of the foreground emissionWe take a simplified approach using the mock 143 GHz channel map with modified amplitudes for the tSZ and CIB Simulations of the CMB data are necessary to computecomponents. kSZ bias is expected to be subdominant (even the final lensing maps [39]. The sparsity of radio sources realizations at the Planck 2018 best-fit cosmology [35] with so means that the bias from this component is expected to potential, which we use to deflect the unlensed CMB map§ince it is not present in the SMICAnoSZ maps. To modify the amplitude of the CIB component, we first generate

We also simulate contributions to the sky from secondamaps of the CIB atall of the frequency channels used to construct the SMICAnoSZ map by scaling the Gaussian CIB realizations at 150 GHz, using the scaling relation based on the CIB map amplitudes in [41] at low frequencies and maps at [42] at higher frequencies. The CIB maps

³A similar result has been obtained by [30] using their LGMCA algorithm based on the blind source separation technique.

⁴As noted in [18], these simulations using Gaussian realizacorrelations, however they are sufficiento estimate the noiselevels and calculating quantities such as the lensing response function.

HFI_RIMO_R3.00.FITS available from the Planck Legacy Archive.

generated this way are then passed through the SMICAnoSZ weights, to generate a mock SMICAnoSZ CIB map. The mock CIB map used in the analysis is finally generated by multiplying the Gaussian 150 GHz CIB map by the multipole-dependentatio of power spectra of the mock SMICAnoSZ CIB map and the Gaussian 150 GHz CMB temperature maps that correlated with the large-CIB map.

C. Combining SPT-SZ and Planck data

In order to capture modes in the SPT-SZ temperature map that are lost due to filtering and to improve the signal known, one could combine multi-frequency CMB obserto-noise of the CMB observations, we combine the SPT-SZations in a way that nulls the contribution from tSZout 150 GHz and Planck 143 GHz maps using inverse variangeserves the underlying CMB signal However, for the weighting. Planck data are used to fill in the spherical harmonic modes I < 500 as well as modes with m < 250. Modes where both SPT-SZ and Planck are noise dominated se than the originaltSZ-biased mapsSince the noise (1 > 1600 and m < 250) are filtered out.

average 2D noise power spectrum hill j²i, where N_{im} are the coefficients of the sphericaharmonic decomposition of the noise map. The SPT-SZ 150 GHz and Planck Several approaches have been proposed in the 143 GHz maps are then combined (we denote the combined map with the superscript x) using the same inverse noise weighted combining techniqué as used in [20,21,43]:

$$T_{lm}^{x} \hspace{0.1cm} \frac{1}{4} \frac{w_{lm}^{SPT}}{w_{lm}^{SPT} b} \hspace{0.1cm} w_{lm}^{Planck} \frac{T_{lm}^{SPT}}{T_{lm}^{SPT}} b \hspace{0.1cm} \frac{w_{lm}^{Planck}}{w_{lm}^{SPT} \hspace{0.1cm} b} \hspace{0.1cm} w_{lm}^{Planck}}, \hspace{0.1cm} \delta 1 \hspace{0.1cm} b \hspace{0.1cm} b \hspace{0.1cm} w_{lm}^{SPT} \hspace{0.1cm} w_{lm}^{SP$$

where T_{Im} are the temperature spherical harmonic coefficients and w_{lm} are the weights per mode, which are taken to be w_{lm} 1/4 1=hj N_m j²i. T_{lm}^{SPT} ; b Planck are the SPT-SZ transfer function (a combination of the beam and filter transfer function) and the Planck beam, respectively. Once the high-resolution SPT-SZbPlanck maps are produced, point sources detected by SPT-SZ with flux O_{L}^{TT} p hj N_{lm} j^2 i p^{-1} , such that T_{lm} $\frac{1}{4}$ F_{lm} T_{lm} $\frac{1}{4}$ T_{lm} = F in the range 6.4 < F < 200 mJy (6.4 < F < 50 mJy)for simulations) are inpainted using the Gaussian constrained inpainting method [20,44,45] out to 3 and 5 arcminutes for sources below and above 50 mJy respectively.

We similarly compute the combined noise power using

$$N_{lm}^{x} \hspace{0.1cm} \cancel{1}_{4} \frac{w_{lm}^{SPT}}{w_{lm}^{SPT} \hspace{0.1cm} b \hspace{0.1cm} w_{lm}^{SPT}} \frac{N_{lm}^{SPT}}{T_{lm}^{SPT}} b \hspace{0.1cm} \frac{w_{lm}^{Planck}}{w_{lm}^{SPT} \hspace{0.1cm} b \hspace{0.1cm} w_{lm}^{Planck}} \cdot \hspace{0.1cm} \tilde{o}_{2} b_{lm}^{Planck} \cdot \hspace{0.$$

We increase the number of simulations from 200 to 300 realizations in the present tudy. The number is limited by the number of FFP10 noise realizations available.

D. Construction of an unbiased CMB lensing map from SPT and Planck data

1. Bias from the thermal Sunvaev-Zel'dovich effect

The tSZ effect induces a frequency-dependent signal into scale structure. As shown in [18,46], this signal can propagate through the standard quadratic estimatosed to estimate CMB lensing, resulting in a bias to correlations between CMB lensing maps and galaxies or galaxy lensing. In principle, since the frequency-dependence of the tSZ is noise levels of SPT-SZ datacarrying out this procedure results in a tSZ-cleaned map thatas significantly higher level in the reconstructed lensing map is proportional to the Starting with the 300 noise realizations, we compute the emperature noise level squared, this results in a significant degradation in the signal-to-noise of the CMB lensing crosscorrelations.

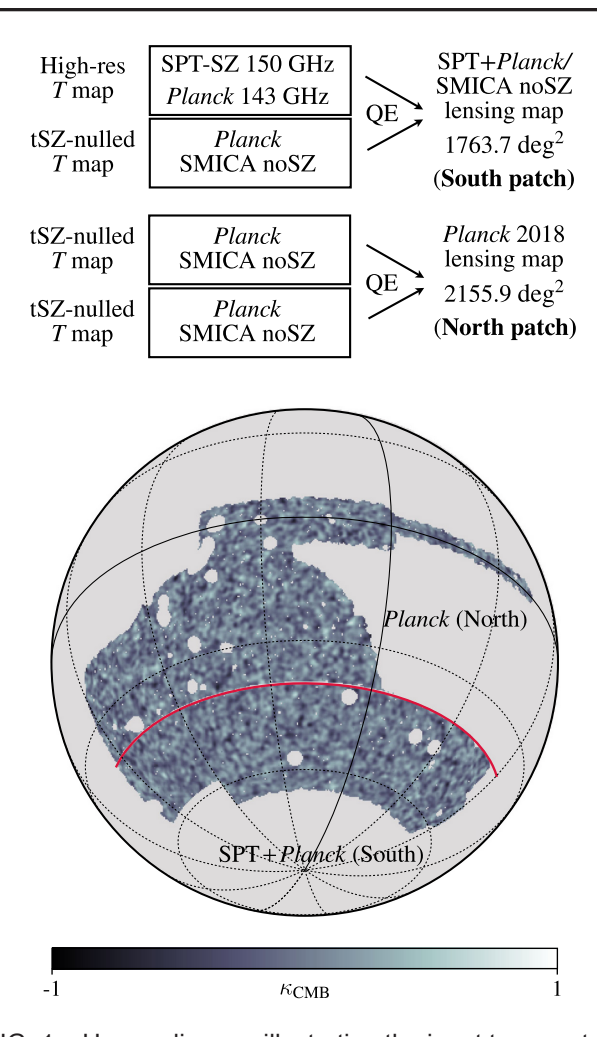
> literature to remove foreground biases in CMB lensing with minimal noise penalty ranging from using a polarization-only lensing reconstruction [47], to using a lensing reconstruction estimatobased on shearinstead of convergence [48]. The approach that we adopt in this work is based on using a modified quadratic estimator [9,46] with two maps, only one of which has been tSZ-cleanedIn effect, by only cleaning one of the maps, the tSZ bias can be removed from the final lensing map, without the high noise penalty incurred from cleaning both maps entering the quadratic estimatorHere we implement the same methodology as [9], but without flat-sky approximations.

2. tSZ-cleaned lensing reconstruction

Prior to running the lensing reconstruction procedure, we filter the temperaturemaps_with the filter F $_{lm}$ 1/4 $\delta C_{I}^{TT} \not = h_{Im} j^{2} i \not= for modes in the range 100 < I <$ 4000 and zero otherwise [20,33,34]. Note here that we use the 1D power spectrum for the signal component, C but use a 2D filtering noise spectrum hillipia to account for possible anisotropies in the noise. The filtering function is also different for T and TSMICAnoSZ since the amplitude of foreground residual and the noise level are different for the two input maps. We then use the quadratic estimator:

where the term in brackets is the Wigner-3j symboland $W_{1,1,2L}^{\phi}$ is the weight function defined as

⁶The weights are publicly available as partof the SMICA weight propagation code at the Planck legacy archive.



CMB lensing maps of [20] could be effectively recovered by replacing the smich solution was the tSZ-free maps for both legs of the estimator (i.e., using $T_{lm}^{SMICAnoSZ}$ for both), the resulting lensing map would also be tSZ-free, but would have higher noise owing to the higher noise levels of the smich and smich maps. References [9,46] have shown that the effect of the tSZ bias can be reduced with a small penalty in signal-to-noise ratio using this technique. We note that the original estimator of [46] used a somewhat uboptimal version of Eq. (3) that was asymmetric in its use of the tSZ-free and tSZ contaminated maps, while [9] introduced a symmetrized version. In principle, one could form a minimum variance combination of the two terms contributing to Eq. (3). However, we do not take this approach because itomplicates the calculation of the estimator and results in insignificant reduction in noise.

We convertthe lensing potential map to lensing convergence,κ, after subtracting the mean field $φ_{LM}^{MF}$ and applying the lensing response function PR

$$\hat{K}_{LM} \frac{1}{4} \frac{L \delta L b 1 D}{2} \delta R_L^{\phi} D^1 \delta \phi_{LM}^- - \phi_{LM}^{MF} D$$
: $\delta 5 D$

Several approaches to obtaining the lensing response function have been proposed. Here we largely follow [20] in that we use the cross-spectrum with the input simulation:

$$R_{L}^{\phi} \frac{hC_{L}^{\bar{\varphi}\phi} i}{hC_{L}^{\varphi\phi} i}; \qquad \qquad \tilde{0}6\dot{P}$$

FIG. 1. Upper: diagram illustrating the input temperature maps used to construct the two different lensing maps utilized in this where φ is the output reconstructed lensing map, the South (SPTbPlanck) patches The red line indicates the cutn declination (dec $\frac{1}{4}$ –40°) that divides the two regions. The union Fig. 2. The calculated noise powerspectrum of the of the DES mask used in the DES Y3 analysis and the Planck lensing map is shown in Fig3. lensing map mask is applied.

analysis. The operation "QE" (quadratic estimator) is the lensing pharred φ are the simulation input lensing potential maps, reconstruction step described in Sec. II D 2. Lower: illustration and the sky coverage and lensing maps for the North (Planck) and the sky coverage and lensing maps for the North (Planck) and tions. Our final reconstructed CMB lensing map is shown

3. Validation of the CMB lensing map

<u>ð2l₁ þ</u> 1Þð2l₂ þ 1Þð2L þ 1Þ $\times C_{l_1}^{TT} = \frac{1 \not b \not \delta - 1 \not b_1 \not b_2 \not b_L}{2} = \frac{1}{1} \cdot \frac{1}{0} \cdot \frac{1}{0} = \frac{1}{0}$ b ðl 1 ↔ l 2Þ; ð4Þ

where the last term implies an identical term with I 1 and I 2 flipped. Equation (3) requires two temperature maps (i.e., the "legs"). Here we use the high resolution SPT-SZpPlanck temperature map T_{lm}^x and foreground cleaned temperature map $T_{lm}^{SMICAnoSZ}$ (see Fig. 1). The

CMB lensing maps, we show stacks of the lensing maps at the locations of tSZ-selected clusters from [22] in Fig. 4. small in SPT-SZ data [49], so we do not expect to see a significant signal at the cluster location. However, as a result of tSZ bias, a significant artefact at the cluster location does appear for the map constructed using the SPTbPlanck temperature maps for both legs of the quadratic estimator (leftpanel). In contrast, when using the SMICAnosz map for one leg of the estimator, no

⁸This will not be a perfect recovery since analysis choices have been changed slightly including the difference in simulations and masking choices.

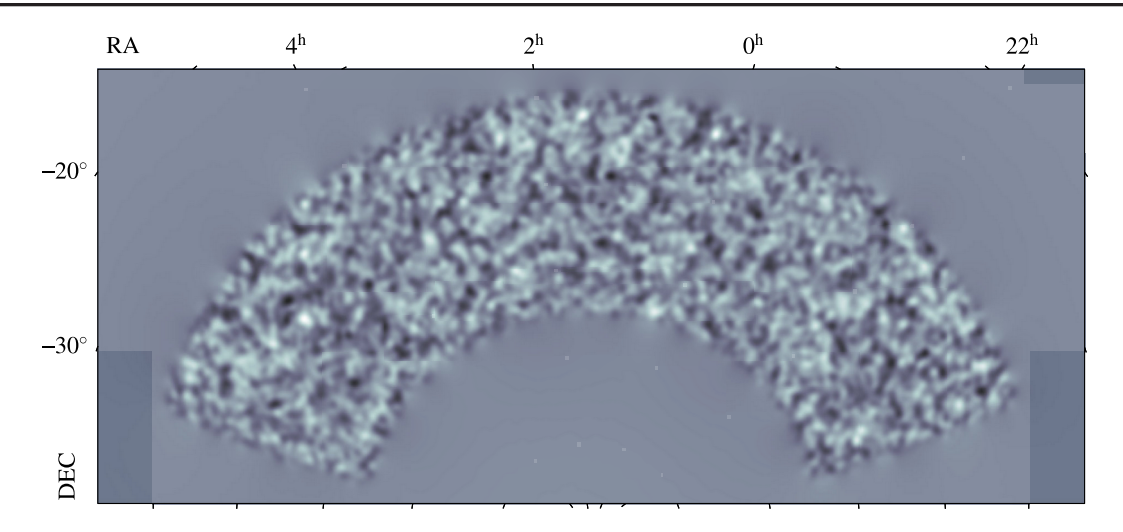


FIG. 2. CMB convergence map generated using the tSZ nulling method described in the text. The map has been smoothed with a Gaussian beam with FWHM 1/4 60 for visualization purposes.

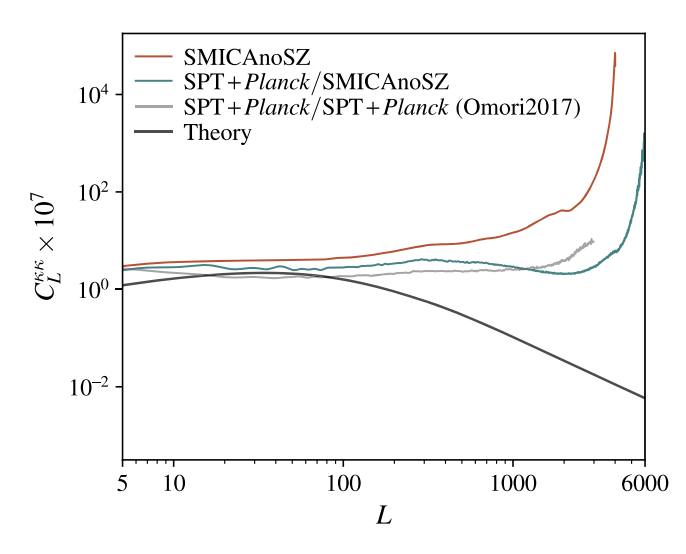


FIG. 3. Noise levels estimated from simulations for SPTbPlanck/SMICAnoSZ (teal) and Planck (orange) over the patch of sky that will be used to measure the cross-correlations. Also shown are the noise levels from [20] (lightgray) and an analytical prediction for the convergence signal (black). The procedures described in Sed. D eliminate tSZ contamination from the lensing maps at the cost of a small increase in the may arying the I max used in the analysis also provides a noise (tealvs. light gray).

significant artefact appears at the cluster location. This suggests thatthe maps produced in this analysis have difference in the noise levels of the two maps, as seen alsoharacterized, which allows us to reach lower L modes in Fig. 3.

We next measure the CMB lensing auto-spectrum and check that it is consistent with that from other studies and theoretical predictions. The formulation of the auto- amplify the CIB in that map (unless the CIB is explicitly spectrum calculation is described in Appendix A, and the nulled, which would result in an additional noise results are shown in Fig. 5. We find that our spectrum is penalty). This could in turn increase the level of CIB

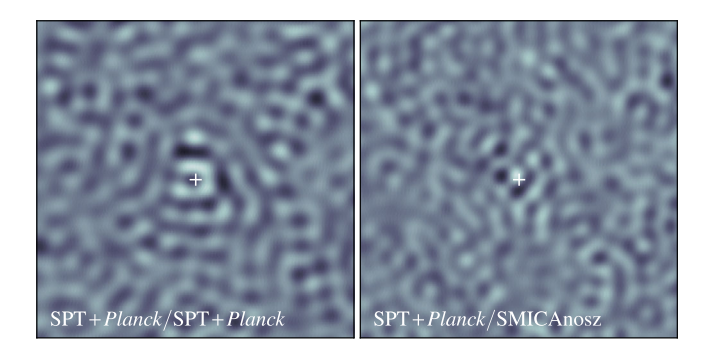
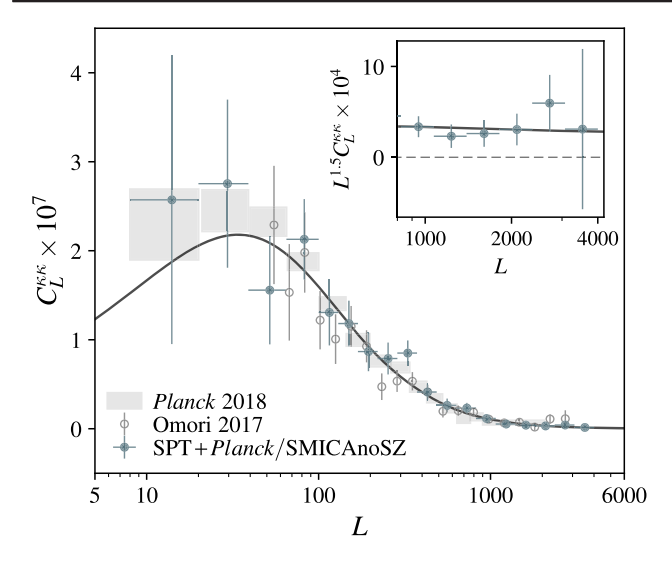


FIG. 4. Stacks of CMB lensing maps at the locations of clusters from [22] with signal-to-noise in the range 5 < S=N < 10. Without tSZ nulling (left panel), the stacked CMB lensing map shows a strong feature at the cluster center due to tSZ contamination of the lensing estimatd/Nith tSZ nulling (right panel), the stacked map shows no strong features that cluster center, as expected since the cluster lensing signal is weak.

highly consistent with other measurement and we find no apparent signatures of foreground contamination. test of foreground contamination [50]; we find no evidence for significant changes in the inferred lensing power spectrum when setting 1/2 2500. We additionally note that due to the inpainting procedure that we carry out prior to the lensing reconstruction, the mask reduced the level of tSZ bias. Note that there is also some becomes less complex, and the mean-field becomes better than in [20].

> The procedure of nulling the tSZ in one of the input temperature maps to the quadratic estimator could



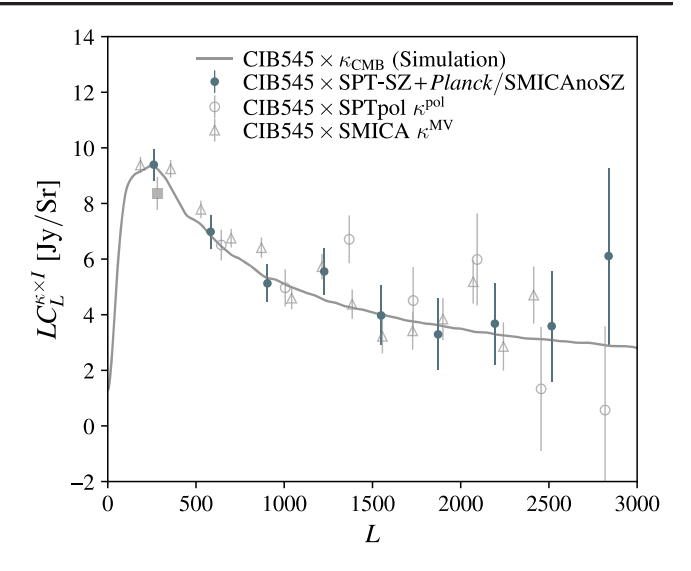


FIG. 5. The power spectrum of the convergence map con-Shown for reference are the points from [16] (gray squares) and orrelation with the SPTbPlanck/SMICAnoSZ lensing map points from [20] (gray open circles), and the analytical convergence power spectrum calculated using the fiducias molthe power spectrum in the high-L range, where possible contamination from the tSZ would show most trongly.

bias in the resultant CMB lensing map. To test whether CIB contamination is significantly impacting our CMB lensing map, we cross-correlate the map with the Planck map at 545 GHz, which is dominated by the CIB. Since the CIB traces large-scale structurewe expect to detect a nonzero correlation (see also Refs. [42,51–55]). We therefore compare our measured κ-CIB correlation with other measurements and predictions from simulations that are known to be uncontaminated by CIB. The rationale behind this testis that any residual CIB contamination of our new lensing maps will correlate strongly with the CIB, causing the crosscorrelation measurement to depart strongly from the predictions of the simulations and previous measurements. To this end, we compare our measurements with (i) cross-correlation between CIB and the minimumvariance lensing map from SMICA (which lower input I max cut of I < 2048 in the lensing reconstruction and is therefore less affected by the CIB bias). (ii) cross-correlation between CIB and CMB lensing map of [56] based on the polarization data from SPTpol (since the polarization of CIB is known to be negligible, the bias is expected to be small), and finally (iii) cross-correlation between CIB and pure CMB lensing in simulations [40].

in Fig. 6, where it can be seen that our cross-correlation measurement is consistent with all the external measure-and CMB lensing convergenceespectivelyWe will also ments. This suggests that CIB contamination is significantly biasing our lensing reconstruction.

FIG. 6. Cross-correlation between various CMB lensing maps structed from the combination of SPT and Planck (blue points) and the 545 GHz map from [42], which is dominated by CIB. The (blue) produced in this analysis is consistent ith other measurements and with an externation (gray curve), demogy assumed in our analysis (black solid line). The inset showsonstrating that this lensing map is not significantly contaminated by CIB.

E. SMICAnoSZ lensing map

Since the SPT-SZ data only reaches up to Dec \(\frac{1}{4} - 40^\circ\), we cover the remaining DES Y3 footprint using the Planck lensing map generated from the SMICA-noSZ temperature map, as shown in Fig. 1. To simplify the nomenclature of the CMB lensing maps used in this analysis, we refer to the SPT-SZbPlanck/SMICAnoSZ map as the "SPTbPlanck lensing map," and the SMICAnoSZ lensing map as the "Planck lensing map" hereafter.

III. MODELING THE CMB LENSING CROSS-CORRELATION FUNCTIONS

The previous section described the construction of CMB lensing map optimized for cross-correlation with DES data. In this section, we describe our modefor the correlations between DES galaxies, galaxy shears and CMB lensing. As mentioned in Sec. I, our modeling framework is largely based on the DES Y1 analysis described in [18], but with several updates to match the analysis choices of the DES Y3 cosmology analysis [57]. We therefore only outline the essentiahodeling components here and refer the readers to the two papers above for details.

For the remainder of the paper, we use γδαnd κ_{MB} to The results of the CIB cross-correlation test are shown refer to the three large-scale structure tracers of interest in this work: galaxy position, galaxy weak lensing (or shear),

⁹Publicly available at https://pla.esac.esa.int/.

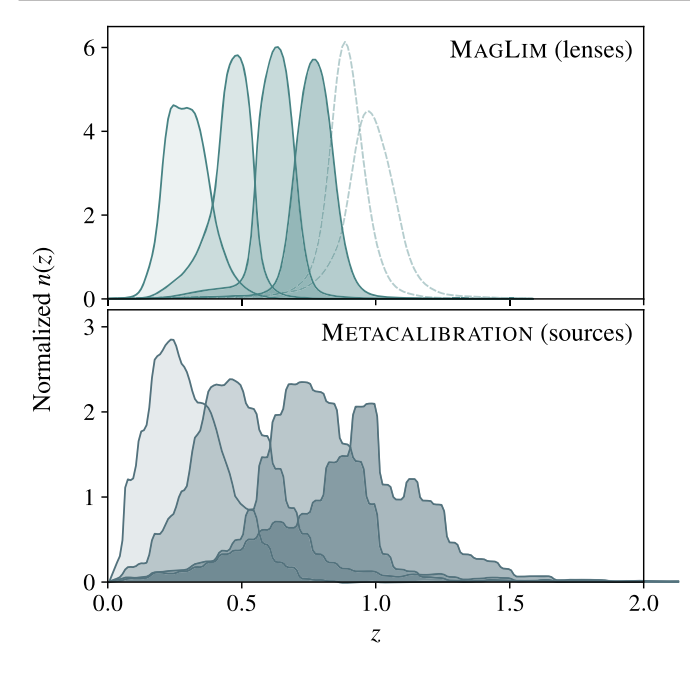


FIG. 7. Redshift distribution for the MagLim lens galaxy sample (upper)and METACALIBRATION source galaxy sample (lower). The highest two redshift bins of the lens sample (in dashed lines) are notice used for the forecasting in this work.

refer to the galaxies that are used for the galaxy density tracers as lens galaxies and the galaxies that have weak lensing shear measurements as the source galaxies. Ultimately, we will consider the full set of six two-point correlation functions between these three fields. Modelingforthcoming data analysis. of correlations between δ_i and γ for DES Y3 data is the modeling of the Planck CMB lensing auto-spectrum.

A. Overview of DES galaxy samples

Unlike analyses with DES Y1 data, the cosmological analyses of DES Y3 data use two different lens galaxy samples: a magnitude-limited sample (MI) [58]) and a luminous red galaxy sample (REDMAGIC [59,60]). The Fig. 7, while the number density of objects are listed in Table I.

There are known trade-offs for each sample. The REDMAGIC sample was found to give internally inconsistent results: the galaxy bias preferred by galaxy-galaxyapproximation [64]: lensing was in conflict with that preferred by galaxy clustering [61]. The MAGLIM sample, on the other hand, were shown to give poor fits to the baseline model, when the highest two lens galaxy redshift bins were included. Given these considerations, the baseline DES Y3 cosmol-

TABLE I. Effective number density of galaxies in each redshift bin for the MAGLIM lens samples as calculated in [15].hese numbers are used to generate the covariance matrix. The highest two redshift bins will not be used for the forecasting in this work.

Lens sample			
Redshiftbin	n _{gal} (arcmin̄ ²)		
1	0.150		
2	0.107		
3	0.109		
4	0.146		
5	0.106		
6	0.100		

TABLE II. Effective number density of galaxies and shape noise for each source redshibtin as calculated in [15].

	Source sample	
Redshiftbin	n _{gal} (arcmin ⁻²)	$\sigma_{\!arepsilon}$
1	1.672	0.247
2	1.695	0.266
3	1.669	0.263
4	1.682	0.314

alternative choices for the lens samples, including the full (i.e., six tomographic bin) MagLim and the REDMAGIC galaxy samplesWe will explore these possibilities in our

The source galaxy sample used in this work is based on described in detail in [57], and we refer readers to that wolfee METACALIBRATION shape catalog described in [62]. The for more details. We refer the readers to [16] for details of galaxies are divided into four tomographic bins and their redshift distributions are inferred via the SOMPZ method [63]; the corresponding distributions are shown in Fig. The number density of galaxies and shape noise estimate for each bin are listed in Table II.

B. Galaxy-CMB lensing cross spectra

We measure two-point functions between the galaxy tomographic bins of the MGLIM lens sample are shown in position, galaxy shape, and CMB lensing observables as a function of angular separation between the points being correlated. To model these correlation, we begin by computing the harmonic-spacecross-spectrabetween CMB lensing and galaxy density/shear using the Limber

ogy results presented in [15] used only the first four bins of here $X \in f\delta_a$; γg , i labels the redshift bin Pbk; $z \triangleright$ is the the MagLim sample, and we will adopt that approach herenonlinear matter power spectrum computed using CAMB for our forecasts. Nevertheless, the methodology developedd HALOFIT [65,66], and χ is the comoving distance to in this paper is general and can in principle be applied to redshift z. As we describe below, Eq. (7) is modified when considering a nonlinear galaxy bias modelThe window functions, q_xð_xÞ are given by

$$q_{\delta_g}^i$$
ðxÞ ¼ bðzðxÞ $p_{\delta_g}^i$ rðzðxÞ $p_{\delta_g}^i$ dz

$$q_{\gamma}^{i}\tilde{\delta}\chi \text{P} \stackrel{1/4}{\cancel{2}} \frac{3H_{0}^{2}\Omega_{m}}{2c^{2}} \frac{\chi}{a\tilde{\delta}\chi \text{P}} \frac{\chi}{\chi}^{\chi_{h}} d\chi^{0} h_{\gamma}^{i}\tilde{\delta}z\tilde{\delta}\chi \text{P} \text{P} \frac{dz}{d\chi^{0}} \frac{\chi^{0}-\chi}{\chi^{0}}; \quad \check{\delta}9\text{P} \frac{dz}{d\chi^{0}} \frac{\chi}{\chi^{0}} \frac{\chi}{\chi^{0}}; \quad \check{\delta}9\text{P} \frac{dz}{d\chi^{0}} \frac{\chi}{\chi^{0}} \frac{\chi}{\chi^{0$$

where H_0 and Ω_m are the Hubble constant and matter density parameters respectivel κόχρ is the scale factor corresponding to $% \left(1\right) =\left(1\right) \left(1\right) \left$ galaxy bias as a function of redshift z, and $n_{\delta_{-}=v}^{i}\delta z$ are the normalized redshift distributions of the lens/source

The angular-space correlation functions are then computed via

$$W^{\delta_{g}^{i}K_{CMB}}\delta\theta P_{4}^{X} = \frac{2l \ b \ 1}{4\pi} F\delta lPP_{l} \ \delta cos\delta\theta P_{2}^{B} C^{MB} \delta lP; \quad \delta 10P_{l}$$

$$w^{v_t^i \kappa_{\text{CMB}}} \delta\theta \text{P} \overset{X}{\not \downarrow} \quad \frac{2 \text{I} \text{ } \text{ } \text{ } 1}{4 \pi \text{I} \delta \text{I} \text{ } \text{ } \text{ } 1 \text{P}} \text{P}_{\text{I}}^2 \delta \text{cos} \; \theta \text{P} \text{F} \delta \text{IP} \overset{\text{C}^{\text{CMB}}}{\bullet} \delta \text{IP}$$

ð11Þ

where P_1 and P_1^2 are the lth order Legendre polynomial and associated Legendrepolynomial, respectively, and FðlÞ describes filtering applied to the κ_{CMB} maps. For correlations with the κ_{CMB} maps, we set Fõlþ 1/4 Bõlþ Θ õl – I $_{min}$ þ Θ õl $_{max}$ – IÞ, where Θ õlþ is a step function and Ball 1/2 the filtering choices (Θ_{FWHM} , I $_{min}$ and I $_{max}$) for the two κ_{CMB} maps are discussed in more detailn Sec.III F.

We calculate the correlation functions within an angularthis analysis are summarized in Table III. bin $\frac{1}{2}\theta_{\text{hin}}$; θ_{max} by averaging over the angular bin, i.e., replacing P δcos θÞ with theirbin-averaged versions P defined by

In the following subsections, we describe individual elements in the modeling framework beyond the basic formalism of Eq. (7).

C. Galaxy bias

The 5 × 2pt analysis with DES Y1 data presented in [17] relied on a linear bias model, where bozp is a constant that 18 We fix be and be to their coevolution values given by 12 different for each lens galaxy redshift bin. That model was -4=7Þðþ- 1Þ and gnl ¼ ðbl - 1Þ [70].

shown to yield unbiased cosmologicationstraints for the data analyzed therein. For the analysis with DES Y3 data, we will use both a linear galaxy bias model and a nonlinear galaxy bias model. As we will show, the nonlinear galaxy bias analysis can be applied down to smaller scales than the linear bias analysis resulting in tighter cosmological constraints.

Briefly, the two models for the galaxy bias, bok; zb, are:

- (i) Linear galaxy bias: We assume that the galaxy bias is independent of scaleola; zÞ ¼ band assume one effective bias value bfor each redshift bin. This is our fiducial analysis.
- Nonlinear galaxy bias: Linear bias is known to break down on small scales [67], motivating the developmentof a nonlinear bias model that will allow us to access information on smaller scales. We follow the implementation of nonlinear bias presented in [61], using an effective 1-loop model with renormalized nonlinear bias parameters [68,69]: b (linear bias), b₂ (local quadratic bias), b_{s2} (tidal quadratic bias) and b_{3nl} (third-order nonlocal bias). This effect impacts any correlation measured using the galaxy density field (i.e., hδ₀δ_ai, hδ₁γ_ti, hδκ_{CMB}i). Effectively it replaces terms like bⁱðzÞR₁ in Eq. (7) with¹⁰

Expressions for the power spectrum kernels, P_2 , etc., are given in [69,71].

The priors and ranges for the values b_1^i and b_2^i used in

D. Lensing magnification

In addition to distorting or shearing shapes of galaxies, weak lensing also changes the observed flux, size and number density of the galaxies—effects referred to as magnification [see e.g., [72]]. Magnification was ignored in the 5 × 2pt analysis with DES Y1 data presented in [17]. Here, we ignore the impact of magnification on the shear-CMB lensing correlation as the impact of source galaxy magnification is expected to be very smallcompared to our statistical precision [57]. We do, however, incorporate the impact of magnification on the galaxy density-CMB lensing correlations. Following [57], we consider the change in projected number density due to geometric dilution as well as magnification effects on

TABLE III. Fiducial and prior values for cosmological and nuisance parameters included in our model. For the priors, U½a; b indicate a uniform prior between a and b, while N ½a; b indicates a Gaussian prior with mean a and standard deviation b. The light faded entri are the values corresponding to the late b bins of the MagLim sample, not used in the fiducial analysis.

Parameter	Prior	Fiducial
Ω_{m}	U1⁄20.1; 0.9	0.3
$A_{\rm s} \times 10^{-9}$	U½0.5; 5.0	2.19
Ω_{b}	U½0.03; 0.07	0.048
n_s	U½0.87; 1.07	0.97
h	U½0.55; 0.91	0.69
$\Omega_{\rm v} h^2 \times 10^{-4}$	U1/26.0; 64.4	8.3
W	U½-2; -0.33	-1.0
a ₁	U½−5.0; 5.0	0.7
a_2	U½-5.0; 5.0	-1.36
η_1	U½-5.0; 5.0	-1.7
η_2	U½-5.0; 5.0	− 2.5
b _{ta}	U1⁄20.0; 2.0	1.0
MagLim		
b ¹⁶	U½0.8; 3.0	1.5, 1.8, 1.8, 1.9, 2.3, 2.3
b ₁ 6	U½0.66; 2.48	1.24, 1.49, 1.49, 1.60, 1.90, 1.90
b ₂ ¹⁶	U½-3.41; 3.41	0.09, 0.23, 0.23, 0.28, 0.48, 0.48
$\begin{array}{c} L_{16}^{16} \\ C_{g}^{16} \\ \Delta_{z}^{16} \times 10^{-2} \end{array}$	Fixed	1.21, 1.15, 1.88, 1.97, 1.78, 2.48
	N ½0.0; 0.7,N ½0.0; 1.1,N ½0.0; 0.6, N ½0.0; 0.6,N ½0.0; 0.7,N ½0.0; 0.8	0.0, 0.0, 0.0, 0.0, 0.0, 0.0
σ_z^{16}	N ½1.0; 0.062N ½1.0; 0.093N ½1.0; 0.054 N ½1.0; 0.051N ½1.0; 0.067N ½1.0; 0.073	1.0, 1.0, 1.0, 1.0, 1.0, 1.0
METACALIBRATION		
$m^{14} \times 10^{-3}$	N ½0.0; 9.1N ½0.0; 7.8N ½0.0; 7.6N ½0.0; 7.6	0.0, 0.0, 0.0, 0.0
$\Delta_z^{14} \times 10^{-2}$	N ½0.0; 1.8N ½0.0; 1.5N ½0.0; 1.1N ½0.0; 1.7	0.0, 0.0, 0.0, 0.0

galaxy flux [73,74] and size [75], which modulate the selection function.

The effect of magnification can be modeled by modifying Eq. (8) to include the change in selection and geometric dilution quantified by the lensing bias coefficients \dot{C}_a .

$$q^{i}_{\delta_{q;maq}} \check{\delta} \chi \dot{\vdash} \, {}^{1\!\!/\!\!4} \, \, \dot{\underline{q}}_{q} \, \check{\delta} \chi \dot{\vdash} \check{\delta} 1 \, \, \dot{\underline{\rho}} \, \, \dot{\underline{\varsigma}} k^{i}_{g} \, \dot{\vdash}; \qquad \quad \check{\delta} 14 \dot{\vdash}$$

where

$$C_g^i \frac{1}{4} 5 \frac{\partial \ln r_g^i}{\partial m} \Big|_{M_{lim}:\Gamma_{lim}} p \frac{\partial \ln r_g^i}{\partial \ln r} \Big|_{M_{lim}:\Gamma_{lim}} - 2; \quad \tilde{o}15p$$

(here m and r represents the observed magnitude and radius respectively) and κ_g^i is the tomographic convergence field, as described in [57]. The logarithmic derivatives are the slope of the luminosity and size distribution at the sample selection limit. The values of these lensing bias coefficients are estimated in [76] and fixed to the values listed in Table III.

E. Intrinsic alignments

The 5 × 2pt analysis with DES Y1 data considered the nonlinear alignment model [NLA, [77,78]] for galaxy intrinsic alignments (IA). For the present analysis, we adopt the more flexible tidal alignment tidal torquing model (TATT) of [79] to describe IA; more details of this model and its implementation in the context of DES Y3 cosmology analyses can be found in [57]. In this model, the intrinsic galaxy shape $\tilde{\gamma}_{\alpha;IA}$, measured atthe location of source galaxies,can be written as an expansion in the density δ_n and tidal tensor s_0 , which can be decomposed into components s_0 .

$$\tilde{\gamma}_{\alpha:|A}$$
 $^{1/4}$ $A_1s_{\alpha} \triangleright A_{1\delta}\delta_m s_{\alpha} \triangleright A_2\delta s \times s_{\beta} \triangleright : \delta 16 \triangleright$

The coefficients for the three terms in Eq. (16) can be expressed as follows:

$$A_1 \tilde{\delta} z \not \triangleright \frac{1}{4} - a \stackrel{-}{C}_1 \frac{\rho_{crit} \Omega_m}{D \tilde{\delta} z \not \triangleright} \frac{1 \not \triangleright z}{1 \not \triangleright z_0} \stackrel{\eta_1}{} \qquad \tilde{\delta} 17 \not \triangleright$$

$$A_{1\delta}$$
ðzÞ ¼ b A₁ðzÞ ð18Þ

$$A_2 \delta z \triangleright \frac{1}{4} 5 \stackrel{\frown}{\underset{p}{c}} \frac{\rho_{crit} \Omega_m}{D \delta z \stackrel{\beta}{\underset{p}{\beta}}} \frac{1 \not p z}{1 \not p z_0} \stackrel{\eta_2}{\underset{p}{\gamma_2}}; \qquad \delta 19 \not p$$

where $\rho_{crit}~ \space{1pt}{1/4}~ H^2 {=}~ 8\pi G$ is the critical density of the universe, z₀ is a pivot scale fixed by convention C₁ is a normalization constant, which is fixed to C₁ 1/4 5 × 10⁻¹⁴M_☉h⁻² Mpc², and DðzÞ is the linear growth factor.

We use a total of five free parameters to describe A: a η_1 , a_2 , η_2 , and b_{ta} and use flat priors as summarized in Table III.

F. Smoothing of the CMB κ map

The noise powerspectrum of the CMB lensing maps increases in amplitude at small scales. Large-amplitude small-scale noise significantly impacts the covariance of the angular-space correlation function measurements thatzing uncertainty in the redshift distributions known as we consider in this analysis, making covariance computa-HYPPERRANK [82], which efficiently marginalizes over tion difficult. To reduce the effect of small-scale noise, wepossible realizations of the redshift distributions. For the apply Gaussian smoothing and low-pass filtering to the the correlation functions but should not bias our analysis because we include the impact filtering in our model. The impact of the Gaussian smoothing amounts to a transformation of the cross spectra:

$$C_I^{\kappa_{CMB}X} \rightarrow C_I^{\kappa_{CMB}X}B_I$$
;

lensing maps we use $_{\text{FWHM}}$ of 6^{0} and 8^{0} respectively We additionally apply low-pass filtering to the maps, with I max 1/4 5000 for the SPTbPlanck lensing map and 1/4 3800 for the Planck-only map. The choice of smoothing scales is made to ensure that the CMB lensing noise in both parameter values, and C is the covariance matrix of maps approaches 0 at rather than blowing up due to the finite resolution of the CMB maps. A dramatic increase given by in noise at small scales would be problematic for our angular-space correlation analysis.

The combination of the filtering and the smoothing ensures that the noise power spectrum of the filtered maps here Poop are the priors on model parameters. We approaches zero at lax.

G. Uncertainty in shear calibration and redshift distributions

We model shear calibration and redshift biases for the DES galaxies as described in [57]. We model shear observed ^{©™BY} is modified by

$$C^{K_{CMB}\gamma^i}$$
 $\delta l P \rightarrow \delta 1 p m^i P C^{CMB}\gamma^i \delta l P;$ $\delta 20 P$

where m is the shear calibration bias for source bin i.

parameters, Δ_z^i , where i labels the redshift bin. This parameter modifies the nozb as

$$n^i \delta z P \rightarrow n^i \delta z - \Delta P$$
: $\delta 21P$

For the lens sample, we additionally introduce a stretch parameter (g) in the redshift distribution such that (combining with the effect above):

$$n^{i} \delta z P \rightarrow \dot{q} n^{i} \delta \dot{q}_{2} z - hzi p hzi - \dot{Q}P$$
: $\delta 22P$

The fiducial values and priors used for σ_z^i and Δ_z^i are summarized in Table III. These choices for the modeling of the lens and source galaxy redshifts are validated in [63,80,81].

We also consider an alternative method for parameter-3 × 2pt analysis presented in [15], HYPPERRANK was CMB lensing maps. This changes the expectation values shown to give similar results as the simpler model shown in Eq. (21). We verify that this is also the case for $5 \times 2pt$ in Appendix C.

IV. MODEL FITTING

We adopta Gaussian likelihoodLðdiðDf.for analyzing the data:

In
$$L\delta d\hat{j}\hat{\theta}\hat{P} = \frac{1}{2}l\hat{d}\hat{-}m\hat{\partial}\hat{P}^TC^{-1}l\hat{d}\hat{-}m\hat{\partial}\hat{P}\hat{P};$$
 $\delta 23P$

where d is the vector of observed correlation function measurements note is the vector of model predictions the data. The posterior on the model parameters is then

summarize the priors on modelparameters in Table III. All values are consistent with those used in [15].

A. Covariance

Computing the likelihood in Eq. (23) requires an estimate of the data covariance matrix. For the block of this matrix calibration biases with a multiplicative factor such that the consisting of DES-only cross-correlations (i.e., 3 × 2pt), we use the halo modelcovariance described in [83] For the blocks involving cross-correlations with CMB lensing, we adopt a lognormal covariance modebased on [83]. We briefly describe the lognormal covariance model below.

In the lognormal model, the galaxy overdensity, galaxy Following [15], our fiducial analysis models the uncer- lensing, and CMB lensing fields are modeled as shifted tainty in the source galaxy redshift distributions with shift lognormal random fields [84]. These are specified by

the so-called shift parameter. The power spectrum of n can signal or noise power to zero; Gnal-noise can be obtained the desired field (computed from our theory model), and µthe total covariance. can be chosen such that hXi ¼ 0, leaving $\hat{\lambda}$ to be specified. Owing to the nonwhite power spectrum of the CMB

λ, and we follow a similar procedure here. In particular, we ompute the noise-noise term in Eq. (28) using many choose the value of λ so that the re-scaled cumulant of the simulations. This approach takes into account he log-normal field,

$$S_3 \delta \vartheta = \frac{h X \delta \vartheta \mathring{B}}{h X \delta \vartheta \mathring{B}^2};$$
 $\delta 26 = \frac{h X \delta \vartheta \mathring{B}}{h X \delta \vartheta \mathring{B}^2};$

matches that predicted by leading order perturbation theory, where ϑ is a choice of smoothing scale-lere we set $\vartheta \frac{1}{4}$ 10, and λ is chosen separately foreach field $(\lambda \frac{1}{4}, 1.089, 1.106, 1.046, 1.252, 1.177, 1.177)$ for the 6 MAGLIM lens redshift bins, λ ¼ 0.866, 1.956, 1.075, 1.1486 for the 5 REDMAGIC lens redshift bins, $\lambda \frac{1}{4} 0.033, 0.085, 0.021, 0.033$ for the 4 sources redshift bins and $\lambda \frac{1}{4}$ 2.7 for CMB lensing field).

The covariance of lognormal weak lensing fields can be written as the sum of a Gaussian contribution and higherorder covariance terms [84]. Reference [83] took these results and generalized them to describe the covariance of here eq; eq are the measured ellipticity components, and arbitrary fields :

$$\begin{split} &C_{LN} \sim C_G \frac{1}{2} \xi_{a_i X_b}; \ \xi_{X_c X_d} \ b \ \frac{\xi_{X_a X_b} \delta \theta_i P \xi_{c_i X_d} \delta \theta_2 P}{A_{survey}} \\ & \times \ \frac{C_S \delta X_a; \ X_c P}{\lambda_a \lambda_c} b \ \frac{C_S \delta X_a; \ X_d P}{\lambda_a \lambda_d} b \ \frac{C_S \delta X_b; \ X_c P}{\lambda_b \lambda_c} \\ & b \ \frac{C_S \delta X_b; \ X_d P}{\lambda_b \lambda_d} \ ; \end{split}$$

where A_{survey} is the survey area (in particular we use the effective overlapping area between the galaxy and CMB surveys), and λ are the shift parameters for the fields a; b; c; d, and Genotes the covariance between two fields only show the decomposition for one redshift bisimilar after the two fields have been averaged overthe entire survey footprint.

Unlike the shot noise and shape noise that impacho γ , respectively, the CMB lensing noise varies strongly as terms for ζ and ζ_{CMB}), and the signal-signal term is larger function of multipole. For this reasonwe adopt a special the covariance matrix. We note that without this treatment, To complete our estimate of the covariance matrix, the covariance validation tests described in Sec. IV B do not must also determine the covariance between the pass. We decompose the total covariance into contributio & The Planck and Planck sky patche and the covariance from signal and noise:

where n is a Gaussian random field with mean zero, and The first two terms can be isolated by setting either the be chosen so that the power spectrum of X matches that by subtracting the signal-signal and noise-noise terms from

PHYS. REV. D 107, 023529 (2023)

References [83,85] describe a procedure for determining noise and the complexities of the DES masket impact of the survey geometry. Furthermore, in the case of the CMB lensing map, since the noise realizations are generated using the real data, this approach captures possible inhomogeneity in the noise overthe sky area. For the lens galaxies, we generate noise catalogs by drawing from the random point catalogs used to characterize the survey selection function. We draw the same number of random points in the survey footprint as the number of galaxies in the data catalog. For the galaxy weak lensing field, we take the data shear catalog and apply a random rotation such thaf86]:

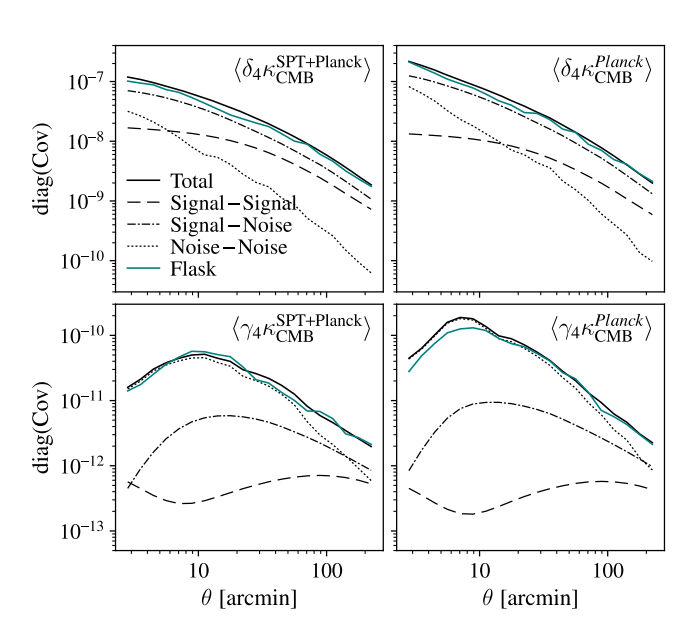
$$e_1^{\text{rot}} \frac{1}{4} e_1^0 \cos \delta 2\phi \triangleright \phi \sin \delta 2\phi$$
; $\delta 29 \triangleright \phi$

$$e_2^{\text{rot}} \frac{1}{4} - e_1^0 \sin \delta 2\phi \triangleright \varphi \cos \delta 2\phi \triangleright;$$
 $\delta 30 \triangleright$

 $\dot{\phi}$ is some random angle between 0 and 2π . We treat these rotated ellipticities as the noise. For CMB lensing, our estimate of noise realizations is formed from the difference between reconstructed lensing maps from simulations (which include noise) and the noiseless input lensing maps that were used to lens the simulated temperature maps. We use 300 noise realizations, since this is the number of noise realizations provided for the Planck lensing maps.

The hδκ_{CMB}i and hytκ_{CMB}i cross-correlations are then measured foreach of the 300 noise realizations and the covariance matrix across these realizations is computed. The relative amplitudes of the covariance contributions as a function of angular scale are shown in Fig8. While we behavior is found for the other redshift bins. Forkhoni, the dominant term at all scales is the signal-noise term (this results from the relative amplitudes of the signal/noise than the noise-noise term at large scales. From hiv most procedure to improve our estimate of noise contributions tof the angular bins are dominated by the noise-noise term. between $h_0 K_{CMB}i$ and $h \gamma_t K_{CMB}i$ with the 3 × 2pt correlations. The covariance between the nonoverlapping SPTbPlanck and Planck sky patches is expected to be small, and we will take the approach of setting it to zero.

¹¹This is an approximation retaining only the first order term after the Gaussian covariance term.



into the various terms in Eq. (28). Results are shown for an arbitrary bin (bin four for both lens and source), but appear similar in other bins. We also overlay the total covariance measured from the FLASK simulations, described in Sec. IV B

The validity of this approximation is tested in the next section. To compute the covariance between அத் and hy κ_{CMB} i with the 3 × 2pt data vector measured over the full DES patch, we rely on the log-normal covariance estimate. We further make the approximation that each patch (SPTbPlanck or Planck) only correlates with the 3 × 2pt measurements over the overlapping fraction of sky through the spectrum caused by baryonic feedback/ve therefore do and that the measurement of the total 3 × 2pt data vector can be expressed as a weighted combination of × 2pt measurements in the different patches. The weights are assumed to be proportional to the corresponding sky areas. This approximation and a similar calculation is discussed in Appendix G of [87]. We show the final correlation matrix for the $h\delta_{KCMB}i$ β $h\gamma_{t}\kappa_{CMB}i$ part in Fig. 9.

We note that the $3 \times 2pt$ analysis presented in [15] included a modification to the covariance matrix which accounts for possible variation in the galaxy-matter corre-matrix recovers the correctx2 distribution from a set of lation at small scales [57]. The galaxy-tangentialshear correlation is a nonlocal quantity such that its value at a given angular scale depends on the galaxy-matter power lensing, and CMB lensing fields (see description of these spectrum down to arbitrarily small scales. Using the technique developed in [88], the analysis in [15] effectivel two-point correlation functions, D_i . The χ^2 is then commarginalizes over a "point mass" contribution to the galaxy-tangential shear correlation at small scales by introducing a modification to the covariance matrixOur analysis of the galaxy-convergence correlation, on the other hand, need not account for a point mass contribution because convergence is a local quantity. One caveat is the the simulations), and C is the covariance matrix the application of smoothing to the convergencemap

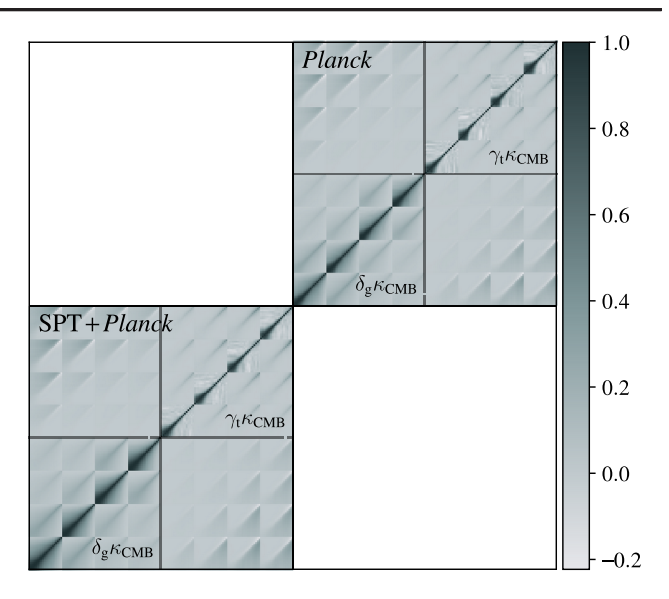


FIG. 9. Plot of the haccmbi þ hγ_tκ_{CMB}i correlation matrix. The off-diagonal cross (SPTbPlanck)-(Planck) blocks are set to zero FIG. 8. Decomposition of the diagonal of the covariance matrix discussed in SetV B 2. Each how Kombi and hykombi block has 80 elements (4 redshiltins with 20 angular bins each).

introduces some nonlocality. However, because our angular scale cuts (see Sec. V) remove angular scales comparable to the smoothing scale, this is not a worry for our analysis. In principle, since the hwcmbi correlation is also nonlocal, we could adjust its covariance to account for a point mass contribution. However, since the signal-to-noise of the hγκ_{CMB}i correlation at small scalesis low, we do not expect this to have a significant impact on our analysis. Furthermore, as we demonstrate in Sec. V, our analysis of hγκ_{CMB}i is robust to variations in the matter power not include a point mass contribution to the covariance matrix for hykcmbi in our analysis.

B. Validation of the covariance matrix

1.
$$\chi^2$$
 test

As a test of the covariance matrix that we obtained in the previous sectionwe first show that using this covariance simulated data vectors. To do this, we first generate simulated realizations of the galaxy position, galaxy weak simulations below). For each simulation, i, we calculate the puted via:

$$\chi_i^2 \frac{1}{4} \delta D_i - M P^T C^{-1} \delta D_i - M P_i;$$
 $\delta 31 P$

where M is the true correlation function (which is known described in Sec.IVA. If C is indeed a good estimation

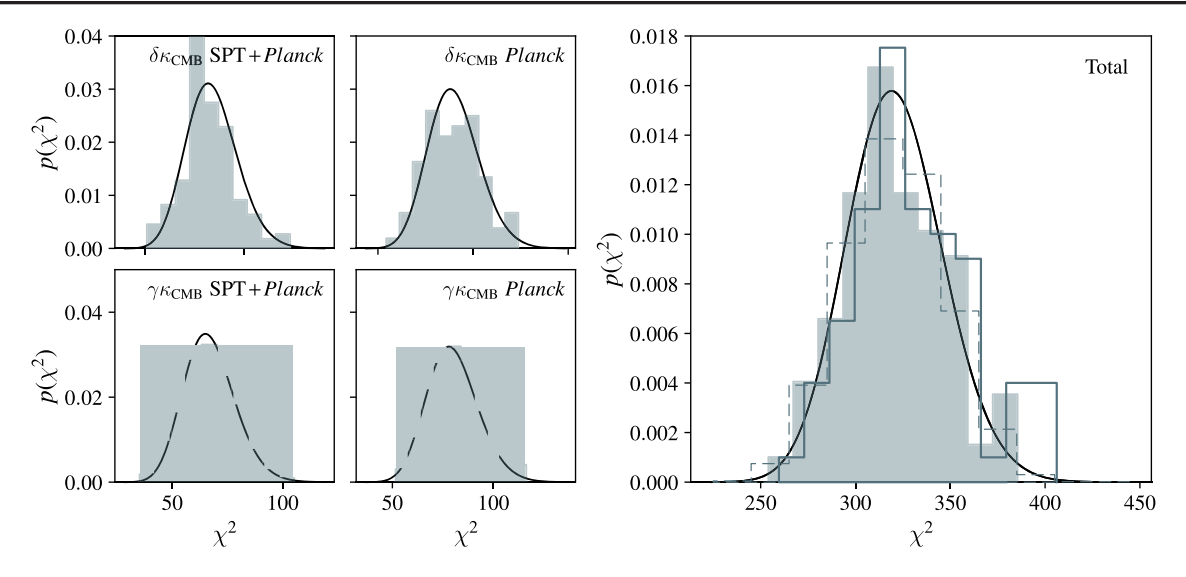


FIG. 10. Left: distribution of χ derived from FLASK simulations and our covariance model for χ derived from FLASK simulations and our covariance model for χ derived from FLASK simulations and our covariance model for χ derived from FLASK simulations and our covariance model for χ derived from FLASK simulations and our covariance model for χ derived from FLASK simulations and our covariance model for χ derived from FLASK simulations and our covariance model for χ derived from FLASK simulations and our covariance model for χ derived from FLASK simulations and our covariance model for χ derived from FLASK simulations and our covariance model for χ derived from FLASK simulations and our covariance model for χ derived from FLASK simulations and our covariance model from FLASK simulations are considered from FLASK simulations and our covariance model from FLASK simulations are covariance model from FLASK simulations and our covariance model from FLASK simulations are considered from FLASK simulations and our covariance model from FLASK simulations are considered from FLASK simulations and our covariance model from FLASK simulations are considered from FLASK simulations and our covariance model from FLASK simulations are considered from FLASK simulations and our covariance model from FLASK simulations are considered from FLASK simu the SPTbPlanck and Planck patches separately. The histograms are overlaid ditatabution (smooth black curve), and we only include data points after the scale cuts (see Sec. V). Right: same as the left panel but for the combined data veotografiant hyκ_{CMB}i in both patches (filled histogram). The open gray histogram represents distribution prior to applying the 4% correction and the dashed histogram corresponds to the distribution when combining different realizations for the SPTbPlanck and Planck patches effectively nulling the off-diagonablock of the covariance in the FLASK realizations, described in Sed. B 2.

of the covariance matrix for D, we expect the distribution of Eqs. (29) and (30) on the DES Y3 galaxy shape χ_i^2 to follow a χ_v^2 distribution with v equal to the dimensionality of D.

This procedure tests several spects of the covariance CMB lensing noise is uniform across the SPTbPlanck and etween the reconstructed lensing map and the input Planck patches is a good approximation (which is assumed invergence map to the noiseless EASK CMB lensing for the signal-noise term in the covariance), since the Second, this test validates our assumption that crosscovariance between observables computed from the SPTbPlanck and Planck patches of the CMB lensing of survey geometry is sufficient to model the data covariance. We note when computing the $\frac{2}{3}$ in these tests we impose angularscale cuts thatremove small-scale mea-

The simulated data used for the 2 covariance testare generated from log-normal realizations of the lens catalogin the analysis. The results of the covarian of the lens catalogin the analysis. (galaxy position), the source catalog (galaxy position and shape), and the CMB lensing map using the package FLASK [89]. We startwith generating a setof noiseless maps of the galaxy density, galaxy lensing and CMB lensing fields given all the combinations of auto- and cross-correlation power spectrum @s well as lognormal shift parameters associated with each field. The lens catalog is generated by Poisson sampling with expectation N ¼ not b δÞ, where n is the average galaxy density per pixel, and δ is the density field generated by FLASK (which 12 We note that this is a good approximation in the weak lensing already includes the galaxy bias For the source catalog, we use the same random rotation approach described

catalog [62]. Shape noise obtained this way is added to the shear signalextracted from the FLASK galaxy weak lensing maps evaluated at the locations of observed calculation. First, it ensures that our approximation that the alaxies 12 For the CMB lensing map, we add the difference map, then apply the same filtering and smoothing to the simulated data vectors include nonuniformity in the noise.maps as the data (described in Sec. III F). We then compute the hδκ_{CMB}i and hγκ_{CMB}i data vectors from these simulations, and evaluate the $\frac{1}{2}$ with respect to the fiducial model as in Eq.(31).

realizations, we have found that the distribution is marginally skewed toward higher $\frac{2}{3}$ than we would expect. To alleviate this, we have scaled up the havi covariance by surements. These cuts will be described in the next sectionsmall amount (4%) such that the distribution matches with expectations, and we subsequently use this covariance test are shown in Fig. 10. The four panels on the left show the χ^2 distributions separately for the two patches of sky and for hδκcmBi and hγκcmBi (combining all redshift bins). We see that individually, all of them show good agreementwith an analytical χ^2 distribution. The right panel shows the χ^2 distribution for the combined data

regime. Formally, the galaxy ellipticity changes under an applied shear according to e.gEq. (4.12) of [72].

two patches of the sky and between the i and hykemei.

we have assumed that the covariance between the patches CMB lensing auto-spectrum measurements to zero. zero (i.e., the empty blocks in Fig. 9). We further test this the difference between these two likelihoods∆ In L, is assumption using the FLASK data vectors. The full FLASK data vector includes the correlation between the patches since they were measured from catalogs generated rameter values listed in Table IIWe expect that as we from the same sky realization. We create a set of "shuffled onsider parameter values farther away from this fiducial data vectors, in which the SPTb Planck patch data vectors hoice, the Δ ln L will increase. However, since we are from one sky realization are combined with the Planck patch data vectors from a different realization, and we compute \forall or each of these sets of shuffled data vectors and original (correlated) data vectors The comparison of the two χ^2 distributions is shown in Fig. 10. We see no significant differences in the two distributions, and we

3. The independence of 5 × 2pt and Planck fullsky

The end goal of this analysis is to perform a joint analysis of the 5 × 2pt data vector and the CMB lensing autospectrum as measured by Planc&ince the sky area that the degree of correlation.

There are several reasons to expect the covariance between the full-sky CMB lensing auto-spectrum from Planck and the 5 × 2pt data vector to be negligibleirst, $z \sim 2$. The 5 × 2pt data vector the other handis most sensitive to structure at ≤ 1, because this is the regime probed by DES galaxy positions and shapes. Second, thenclude SR information as a separate likelihoods done bulk of information in the Planck CMB lensing autospectrum analysis is derived from outside the patch of sky over which we measure 5 × 2pt—the overlap is approximately 15% of the Planck lensing analysis area. Finally, we note that over the SPT-SZ patch bulk of the lensing information comes from SPT-SZ data, hich has instrumental noise that is uncorrelated with the Planckider in this analysis are impacted by several physical observations.

To determine whether the covariance between 5 × 2pt and the Planck lensing auto-spectrum can be ignored, covariance between the 5 × 2pt and full-sky CMB lensing reach the ten percentevel [91,92]. Fully capturing feedlation described in Sec. IVA. We must account for the facthe complexity and large dynamic range of the problem. that 5 × 2pt is measured over a small patch of sky, while the ce this astrophysical street impacts the matterpower full-sky. To do this, we make the approximation that

vector, which includes the cross-covariance between the inside the DES patch and outside of that patch, and that the covariance between 5 × 2pt and the outside-the-patch CMB lensing auto-spectrum measurements can be ignored.

2. The independence of SPT + Planck and Planck patches Once the full 6 × 2pt covariance has been computed, we compute the likelihood of a 6 × 2pt datavector with and In the covariance we described in the previous section, without setting the cross-covariance between 5×2 ptd small, then we can ignore the cross-covarianc€.or this purpose,we generate a 6 × 2ptdatavector at the fiducial generally only interested in the parameter volume near the maximum likelihood, an increase in Δ ln L at extreme parameter values is not problematic. We find that for loglikelihoods within about 50 of the maximum likelihood. $\Delta \ln L \lesssim 0.2$. Such a small change in the likelihood will not significantly impact our parameterconstraints. We are conclude that the ignoring the off-diagonal blocks is valid therefore justified in ignoring cross-covariance between 5 × 2pt and the full-sky CMB lensing auto-spectrum.

C. Shear ratio information

As described in [15], ratios of galaxy-lensing correlation functions that use the same lens sample, but different DES observes lies within the sky area that was used for tleource galaxy samples can be used to constrain e.g., source Planck CMB lensing analysis, we expect the measurements and intrinsic alignment model parameters. to be correlated to some degree. In this section, we examisince such ratios are essentially independent of the galaxymatter power spectrumthese ratios can be used attuch smaller scales than are employed in the standard 3 × 2pt analysis [90]. We refer to these lensing ratios as shear ratios (SR). The analysis presented in [15] treats the SR inforthe CMB lensing auto-spectrum is most sensitive to redshiftation as a separate likelihood that can be combined with the likelihood from the measured two-point functions.

> Our fiducial analysis of the 5 × 2pt observable will in [15]. A detailed description of the DES Y3 implementation of SR can be found in [90].

V. CHOICE OF ANGULAR SCALES

The cross-correlations with CMB lensing that coneffects at small scales (k ≥ 0.2h Mpb) that are challenging to model. For one, feedback from active galactic nuclei (AGN) impacts the distribution of baryons on small scales, proceed as follows. First, we compute the theoretical crosleading to changes in the matter power spectrum that can angular-space auto-spectrum using the log-normal formu-back physics in an analytic model is very challenging given CMB lensing auto-spectrum is measured over (nearly) the pectrum, feedback will necessarily have an impact on both hδκ_{CMB}i and hγκ_{CMB}i. Another small-scale effect that we the full-sky CMB lensing measurements can be expressednust contend with is a breakdown in the linear bias model as an inverse-variance weighted average of measurements use to describe the clustering of galaxies. At small

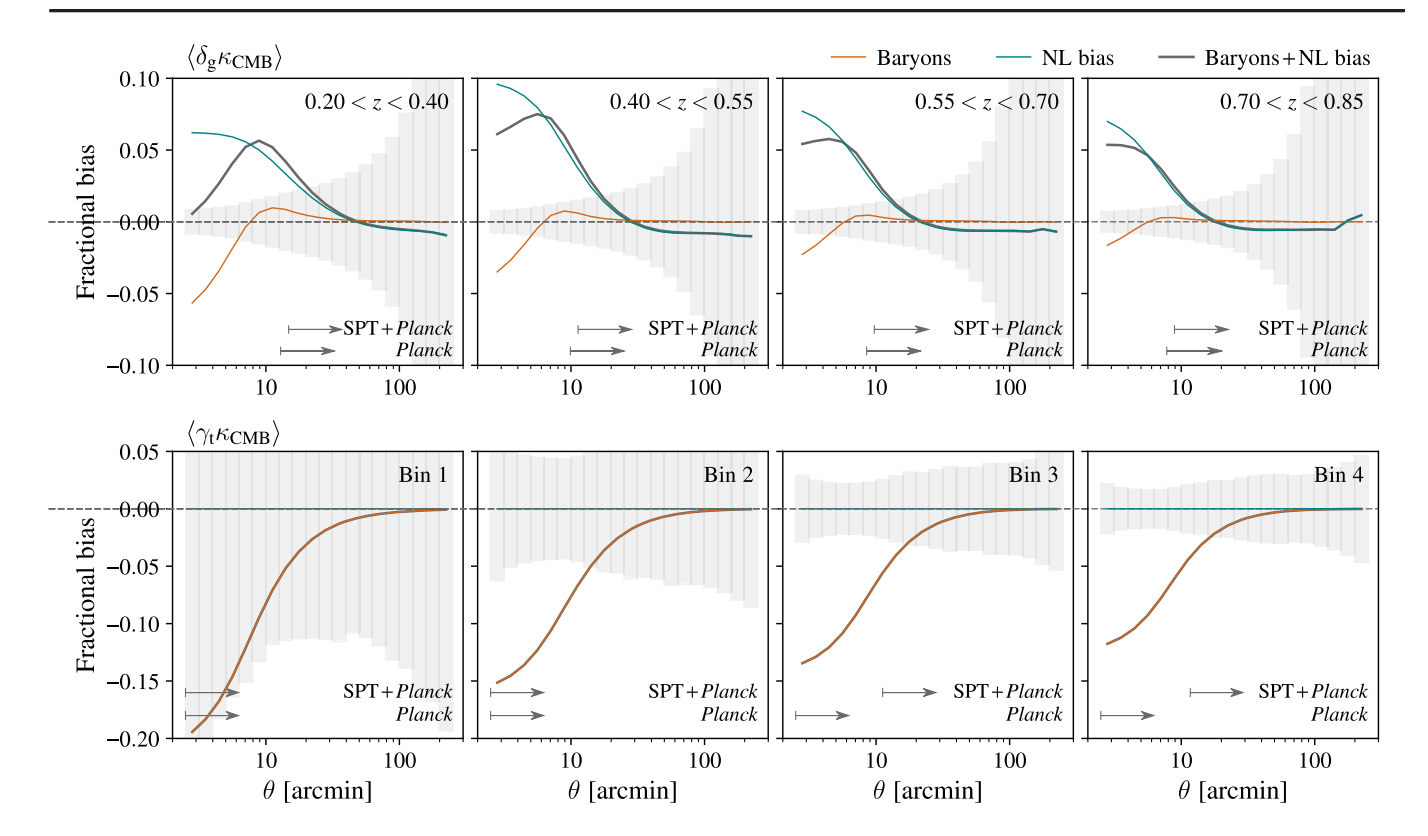


FIG. 11. Fractional biases computed from the contaminated/uncontaminated data vectors with the effects of baryonic effects on the matter power spectrum (orange), nonlinear galaxy bias (teal), and the sum of the two (dark gray). Also shown are the standard deviati of the SPTbPlanck data vectors scaled down by a factor of 10the arrows indicate the angular scales used in the analysis.

scales, galaxy bias becomes nonlinear [93]. Nonlinear galaxy bias will impact hδικ_{CMB}i (see discussion of a nonlinear bias model in SedII C).

those physical scales that are least impacted. In general, AGN model [94]; for nonlinear bias,we adopt the model corresponds to restricting the analysis to large physical in their analysis of correlations of DES-only correlation functions, and we do the same here. This approach is conservative in the sense that it is largely robust to detailednsistent with other DES Y3 analyses. assumptions about feedback and nonlinear bias. Of course, We note that the analysis of cross-correlations between it also comes at the cost of reduced signal-to-noise.

We now develop a choice of angular scales to include itensing presented in [17] also took the approach of our analysis of hδ_tκ_{CMB}i and hy_tκ_{CMB}i. Throughoutthis discussion,we refer to effects such as baryonic feedback and nonlinear bias which are not modeled in our analysis asted previously, one of the main sources of bias in that the analysis from unmodeled effects should be minimized the signal-to-noise. In the present analysis, because we which requires excluding small angular scales from the analysis. Second, we would like to maximize our constraining power, which motivates including more angular retained. scales in the analysis. To set a balance between these two The impact of baryonic feedback and nonlinearbias

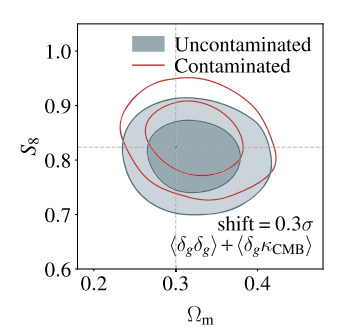
uncertainties.

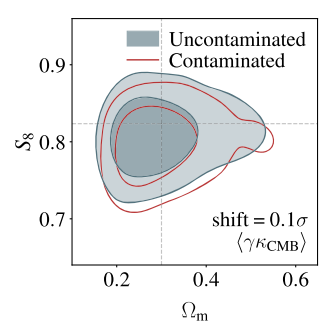
In order to estimate the biases in our constraints caused by unmodeled effects and to make an appropriate choice of angular scales to include, we must have some (at The impact of baryonic feedback and nonlinear bias onleast approximate) guess at the impact of these effects. our analysis can be reduced by restricting the analysis to Following [57], for baryonic feedback, we adopt the OWLS

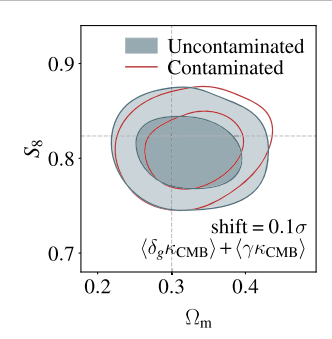
described in Sec. III C. Once the bias has been estimated, scales. The 3 \times 2pt analysis of [15] has taken this approacher requirement is then that there is less than a 0.3 σ shift in the S_8 - Ω_m constraints relative to the constraints obtained using the uncontaminated data vector. This criterion is

DES Y1 data and SPT/Planck measurementsof CMB removing small angular scale measurements in ordeto obtain unbiased cosmological constraints. However, as "unmodeled effects." The choice of angular scale cuts is analysis was from tSZ contamination of the CMB lensing motivated by two competing considerations. First, biases to aps. This bias necessitated removal of a large fraction of have endeavored to make a CMB lensing map that is free from tSZ bias, a larger fraction of the signal-to-noise can be

considerations our requirement is that the bias caused by on the $h_{\delta_t} \kappa_{CMB}$ and $h_{V_t} \kappa_{CMB}$ data vectors is shown in unmodeled effects should be significantly smaller than ouFig. 11. It is apparent that baryonic feedback suppresses the correlation functions at small scales, and has a larger impact







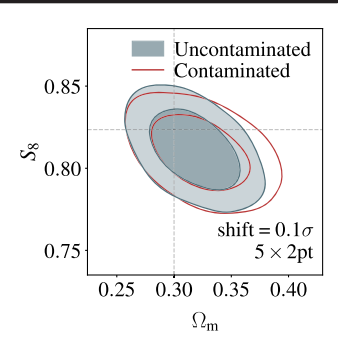


FIG. 12. Forecasted constraints on and S using the fiducial data vector (blue) and a data vector contaminated with our model of nonlinear galaxy bias and baryonic effects on the small-scale matter power spectrum (red). The four panels show (from left to right) results for the combinations of $\mathbf{\delta}_{\mathbf{q}}$ \mathbf{b} \mathbf{b} \mathbf{b} \mathbf{b} \mathbf{c} _N_{KCMB}i, hγ_tκ_{CMB}i, hδ_qκ_{CMB}i \mathbf{b} hγ_tκ_{CMB}i and 5 × 2pt. The shift in the two contours are shown in the bottom right of each panel.

on hy κ_{CMB} i than h $\delta_{\alpha}\kappa_{CMB}$ i. Nonlinear bias,on the other hand, leads to an increase in hand, has no impacton hykcmbi (since the latter does notuse galaxies as tracers of the matter field). The fact that hδκ_{CMB}i and hγκ_{CMB}i are most impacted by different presents a complication. This ensures that the biases to cosmological parameters caused by unmodeled effects in motivated than for h&cmb. Instead, we remove angular hδ_{κ_{CMB}}i and hγκ_{CMB}i typically act in opposite directions, and to some extent will cancel each other in a joint analysistased and unbiased data vectorshis results in keeping of both haκ_{CMB}i and hγκ_{CMB}i. In principle, this cancellation means that we could use very small angular scales in the smallest scales for bin 3 (4) for the SPTbPlanck logical constraints. However, ince the adopted models of constraints on the Ω_m – S_8 plane using the $h \delta_R \kappa_{CMB} i \beta$ nonlinear bias and baryonic effects also have associated uncertainties, we investigate the two biases separately.

In determining the scale cutswe first choose the scale cuts for hockets such that the inclusion of nonlinear bias in the joint analysis of hgκ_{CMB}i and hδ_qδ_qi results in an acceptably smallbias to the cosmological posterior. By considering hard and hard together, we maximize the impact of nonlinear bias (which would lead to a conservative scale cut)and also ensure that galaxy bias is well constrained. Our scale cuts for Ino are based on a physical scale evaluated at the mean redshift of the leastlinear bias is not an unmodeled effect, we follow a galaxies. The minimum physical scale is then translated into angular scales for each of the lens galaxy binsWe consider differentscale cuts for the correlations with the SPTbPlanck and Planck-only CMB lensing mapssince the scale cuts applied, we run a simulated likelihood analysis with the $h\delta_a\delta_a$ i β $h\delta_a\kappa_{CMB}$ i combination using the framework described in Se&V. As shown in the left panel of Fig. 12, we find in the case of the linear bias analysis that a choice of 4 Mpc for SPTbPlanck and 3.5 Mpc for Planck-only meets our acceptability criteria fo@nalysesof h&κ_{CMB}i and hyκ_{CMB}i are summarized in the bias in cosmology, while maximizing signal-to-noise ratio. Our definition of acceptable bias is that the maximum the case of the linear bias analysis, for the hδικ_{CMB}i posterior point of the biased posterior should enclose at

p ffiffiffi most erfő0.3= 2Þ of the unbiased posteriomass in the Ω_{m} - S_{8} plane (marginalizing over albther parameters).

We next choose angular scales for that the joint analysis of h κ_{CMB} i and h $\delta_i \kappa_{CMB}$ i remains unbiased. Since the hwcmbi measurements at a single angular scale biases, and that these two biases act in opposite directionsorrespond to a wide range of physical scales, choosing a hγκcmBi scale cut based on a physical scale is less scales in order of their contribution to the 2/2 between the most of the hkcmbi data vector except for 6 (8) data points our analysis without sustaining a large bias to the cosmo-patch. We show in the middle panel of Fig. 12 the resulting hγκ_{CMB}i combination for the contaminated and uncontaminated data vectors. Lastly, we check that our choice of angular scales results in the 5 × 2pt data vector passing the nation of the nonlinear bias and baryonic feedback models. These results are shown in the right panel of Fig2.

We adopt a slightly different procedure to that described above for determining an appropriate choice of angular scale cuts for the analysis that uses the nonlinear galaxy bias model described in Sec. III C. Since in that case. procedure similarto [61] to determine appropriate scale cuts. We determine the scale below which our nonlinear bias model fails to describe the 3D galaxy-matter correlation function in the MICE simulations [95,96]. We describe these correlations have different signal-to-noise ratio. With detail our procedure in Appendix D—we find that a scale cut of 3 Mpc meets our acceptability criteria for the bias in cosmology, while maximizing signal-to-noiseSince nonlinear bias does not impact hykcmbi, we adopt the same scale cuts as described above for analyzingkhmai.

> The final choice of angular scale cuts to be applied to the Table IV, together with the resulting signal-to-noise ratios. correlations, the minimum angular scales when correlating

TABLE IV. Minimum angular scale cuts for իδ_{:MB}i and hγκ_{CMB}i, for both the SPTþPlanck and Planck patches. The maximum scale for all the data vectors is 250 arcminumbers in parentheses correspond to the nonlinear galaxy bias analysis.

Туре	Redshiftbin	θ_{min}		Forecasted S=N		
		SPTþPlanck	Planck	SPTþPlanck	Planck	Combined
h& _{KCMB} i	1 2 3 4 All bins	14.8° (11.0°) 11.3° (8.5°) 9.7° (7.3°) 8.9° (6.6°)	12.9' (11.1') 9.9' (8.49') 8.5' (7.25') 7.7' (6.64')	12.2 (14.9)	11.6 (12.7)	16.9 (19.6)
hұқ _{СМВ} і	1 2 3 4 All bins	2.5° 2.5° 11.2° 17.7°	2.5° 2.5° 2.5° 2.5°	10.1	8.7	13.3
hგκ _{CMB} i þ hγ _t κ _{CMB} i	All bins			13.9 (15.8)	12.6 (13.5)	18.8 (20.8)

SPT/Planck CMB with the lensing map are redshift bins for the linear bias analysis. This reduction, ð14.8; 11.3; 9.7; 8.9 pr the four redshift bins. These cuts which is still significant despite the tSZ-cleaned CMB are necessitated by possible breakdown in the linear galakensing map, is necessitated by possible breakdown in the bias model at small scales. When using the nonlinear biasinear galaxy bias modelt small scales. When using the galaxy model, the corresponding minimum angular scalesnonlinear bias galaxy modelthe corresponding reduction by uncertainty in the baryonic feedback model. The lations with the SPT/Planck map because the signal-tonoise of the Planck-only lensing map is lower. We can compare these angular scale cuts to those used in the DEØth galaxy survey-CMB lensing cross-correlations. Y1 analysis of [17], which were at §15; 25; 25; 15 for redshift bins centered at approximately the same redshiftsperformed for the REDMAGIC sample, and the results are The more aggressive scale cuts in this analysis are madepresented in Appendix E. possible by the tSZ-cleaned CMB lensing map.

The increased range of angular scales afforded by the tSZ-cleaned CMB lensing map is even more significant for hγκ_{CMB}i. In this case, the minimum angular scales are 82.5; 2.5; 11.2; 17.7% r the four redshift bins. As can be seen in Fig. 11, the change in scale cuts across the different redshift bins is driven largely by the increase in signal-to-noise of the hykcmbi measurements athigh redshift. These scale cuts can be compared to those imposed in the DES Y1 analysis of [17], where scale cuts at δ 40; 40; 60; 60 pere imposed for similar redshift scales for the present analysis is enabled by the tSZcleaned CMB lensing map. Because hykcmbi is not impacted by nonlinear bias, but is strongly impacted by tSZ bias, tSZ cleaning has a more significant mpact for this correlation than for hδκ_{CMB}i.

We can also compute the reduction in signal-to-noise caused by the angular scale cuts. Relative to using a minimum scale of 2.5, the adopted scale cuts results in a signal-to-noise reduction for $\hbar \delta_{\rm MB}$ i of 45% across all

are §11.0; 8.5; 7.3; 6% These cuts are in turn necessitated in signal-to-noise is 36%, necessitated by uncertainty in the baryonic feedback modelFor $h\gamma \kappa_{CMB} i$, the reduction in minimum angular scale cuts for the correlations with the signal-to-noise resulting from the scale cuts is 15%. These Planck-only lensing map are reduced compared to corre-numbers highlight that future improvements in modeling of baryonic feedback can enable significaintcreases in the signal-to-noise that can be used for constraining cosmology

The same procedure to determine the scale cuts is also

VI. FORECASTS

We now use the methodology developed above to produce forecasts or cosmological constraints obtained from the CMB lensing cross-correlation functions. hese forecasts will inform our forthcoming analysis with real data.

A. $hδ_i κ_{CMB} i + hγκ_{CMB} i$

The forecasted cosmologicationstraints from the joint bins. Again, the significant reduction in minimum angular analysis of h_δκ_{CMB}i and hγκ_{CMB}i are presented in Fig. 13. Constraints are presented with and withouthe inclusion of shear ratio (SR) likelihood described in Seb/ C. We observe a significant improvement in the constraints when the SR likelihood is included. The improvement is particularly noticeable in the S direction, which is roughly proportional to the amplitude of the lensing power spectrum. This improvement is not surprising since the SR likelihood can significantly improve constraints on IA parameters, as demonstrated in [90,97,98]. We see in

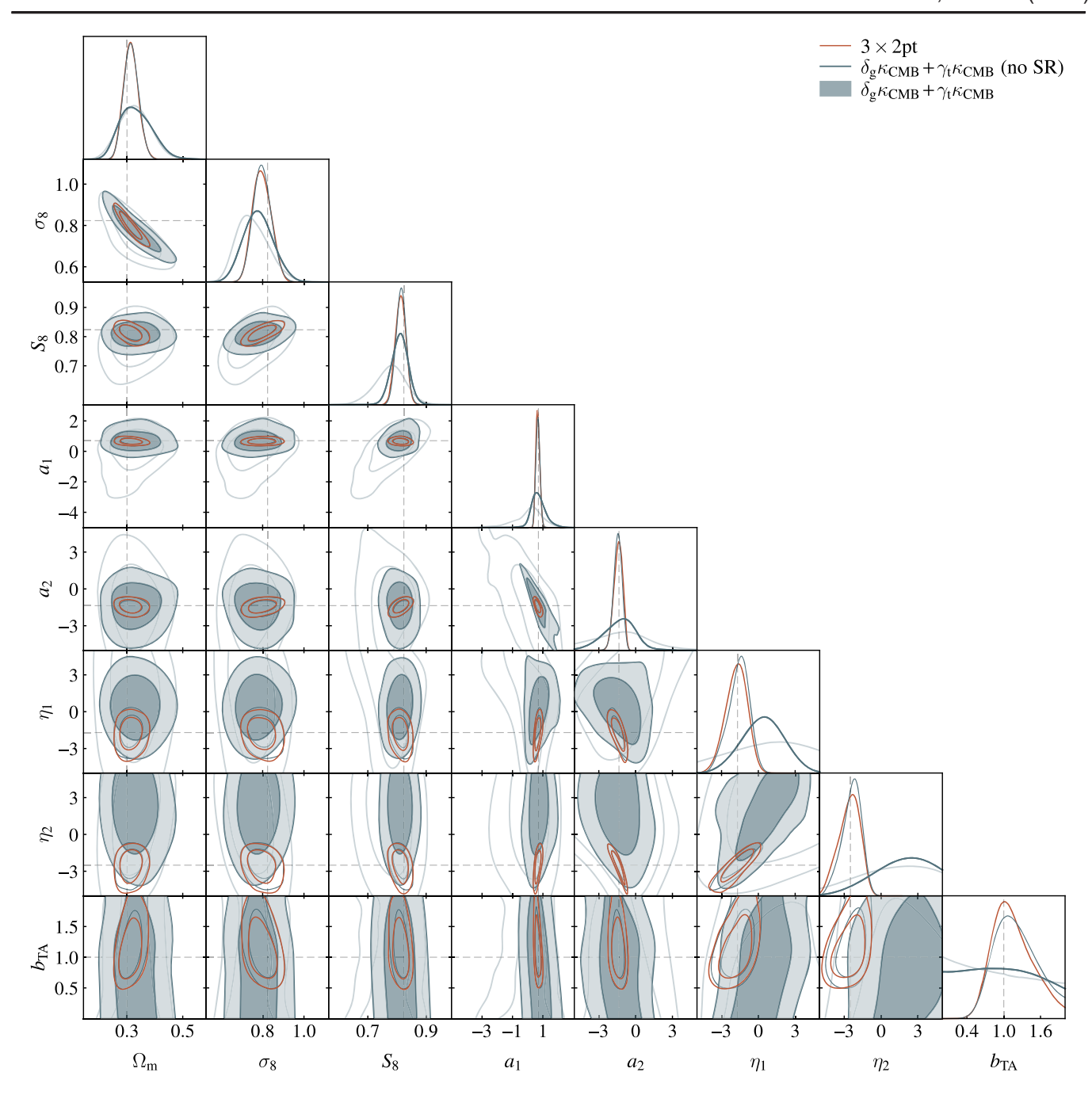


FIG. 13. Comparison of the forecasted constraints on cosmological parameters a, and intrinsic alignment parameters a, η₁, η₂, and β_A using the combination of galaxy clustering and galaxy-CMB lensing correlation, with and without the addition of shearratio information, compared with the constraints from 3 × 2pt. The dashed lines represent the input values for the individual parameter

Fig. 13 the corresponding IA constraints and how a is strongly degenerate with & The SR constraints signifiwhich in turn tightens the cosmological constraints.

significantly larger than that of 3 × 2pt. However, when projecting onto S₀, we expect our cross-correlation concantly reduce the IA parameter space allowed by the datastraints to be only 1.4 times larger than 3 × 2pt, with a 3% level constrainton S_8 . This suggests that the $h \delta \kappa_{CMB} i \beta$

hγκ_{CMB}i combination could provide a powerful consis-For comparison, we also overlay constraints from the 3 × 2pt data combination, analyzed with the same analysitency check for the 3 × 2pt data that is quite independent choices described in this paper. We see that when examinend robust to systematic effects that are only present in the ing the Ω_m – σ_8 plane,our cross-correlation constraints are galaxy surveys.

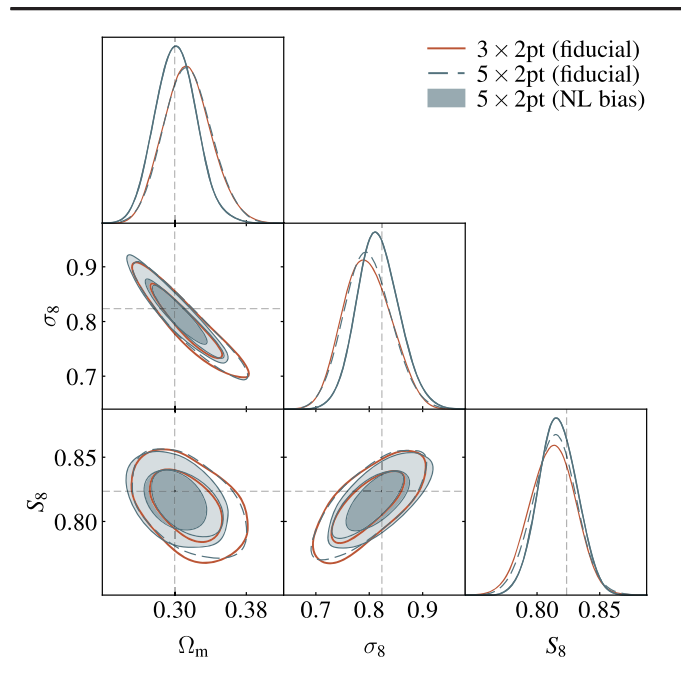


FIG. 14. Comparison of the forecast constraints on Ω and modeling (open orange and dashed blue contours) and nonlineancertainty. As a result, cross-correlations of galaxy surgalaxy modeling (filled blue contours).

B. 5 × 2pt

Next we combine $h_0 \kappa_{CMB}$ i p $h \gamma_t \kappa_{CMB}$ i in the previous section with the 3 × 2pt probes, including the SR likelihood, to arrive at Fig. 14. For reference, we also include the 3 × 2pt constraints on the plot. We observe that although the overall improvement in constraining power over 3 × 2ptis weak, hδ_tκ_{CMB}i þ hγ_tκ_{CMB}i mildly breaks the degeneracy of the 3 × 2ptonstraints to give slightly tighter 5 × 2pt constraints. We expect an improved precision on $\Omega_n = \sigma_8 = S_8$ from 8.3=5.7=2.3% to 8.2=5.4=2.1%. $\bar{\epsilon}$ It is worth emphasizing again that even though the added constraining power is not significant, the mere consistency (or inconsistency) between $h \delta_{CMB} i \rho h \gamma_t \kappa_{CMB} i$ and 3 × 2pt could provide nontrivial tests for either systematics or new physics. This is because the cross-correlation probes include a dataset that is completely independent of all DES $\stackrel{\circ}{\epsilon}_{0.0}$ data processing pipelines, and therefore should not be sensitive to systematic effects that only exist in DES data (and vice versa for CMB datasets). In particular, given the \$\vec{z}\$ somewhatpuzzling inconsistenciesbetween the galaxygalaxy lensing and galaxy clustering signals using the REDMAGIC sample from the DES Y3 3 × 2pt analysis [15], this consistency test will become extremely important for making progress in the future.

In Fig. 14 we also show the forecasted 5 × 2ptcongain in the constraining power compared to the linear galaxy bias mode. The gain in constraining power going from 3 × 2pt to 5 × 2pt when using nonlinear galaxy bias imformed by external priors.

similar to that using linear galaxy bias, with a forecast constraint on $\Omega_m = \sigma_8 = S_8$ going from 7.9=5.2=2.0% to 7.7=4.7=1.9%.

C. Constraints on shear bias parameters

Cosmological constraints from galaxy surveys can be significantly degraded by systematic uncertainties impacting measurements of the lensing-induced shears, and the measurements of photometric redshift for the lensed galaxies. Shear calibration systematics are especially pernicious, since a multiplicative bias in shear calibration is perfectly degenerate with the amplitude of the lensing correlation functions that we wish to constrain [99]. Typically, ancillary data is used to constrain these sources of systematic uncertainty. In the case of multiplicative shear bias, one often relies on simulated galaxy images to constrain the bias parametersm. If the simulations do not accurately capture the properties of real galaxies, priors on m may be untrustworthy.

CMB lensing, on the other hand, provides a measure of S_8 from the 3 × 2pt and 5 × 2pt probes using linear galaxy bias the mass distribution that is independent of these sources of veys with CMB lensing have different sensitivity to the nuisance parameters describing these effects than autocorrelations of galaxy survey observables. By jointly

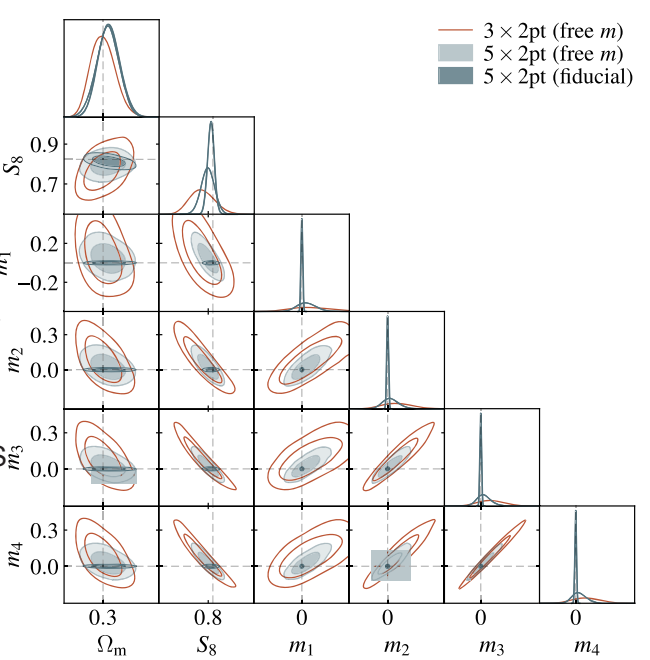


FIG. 15. Simulated constraints from 3 × 2pt (red) and 5 × 2pt (blue) probes when the fiduciabriors on the shear calibration straints assuming nonlinear galaxy bias. We find an overal how the ability of the data to constrain these nuisance parameters with the 3 × 2pt and 5 × 2ptprobes respectively Also overlaid are the fiducial 5 × 2pt constraints, where the parameters are

analyzing the autocorrelations and the CMB lensing crosscorrelations, one can obtain constraints on m directly from the data [12,13,100]The idea of using the data to obtain constraints on nuisance parameters is often referred to as self-calibration.

our new datasets and models. We perform our fiducial 3 × 2pt and 5 × 2pt analyses removing the tight priors on data. These forecasts make use of the true noise levels of the shear calibration parameters in all redshift binsamd replacing them with very wide flat priors. We show in Fig. 15 the constraints in the Ω -S₈ plane as well as the shear calibration parameters. We see that without any prior knowledge of the shear calibration parameter, both 3 × 2pt and 5 × 2ptare able to place constraints on these parameters to some extent: 3 × 2pt measures at the 8% level while 5 × 2pt is expected to significantly improve on that, and constrain \$ at the 4% level.

These uncertainties on m (\sim 0.1 – 0.2 for 3 × 2pt and \sim 0.05 – 0.1 for 5 × 2pt) are still much larger than what we could achieve with other approaches using e.g.şimulations, which are currently below 0.01 [101]. These findings are consistent with our results in [17].

VII. SUMMARY

We have presented the key ingredients foour forthcoming analysis of cross-correlations between DES Y3 measurements of galaxy positions and galaxy shearsd measurements of CMB lensing from SPT and Planck data. These include:

- (1) A new CMB lensing map that is constructed to remove bias from the thermal SZ effect using a combination of SPT and Planck data in the SPT-SZ footprint. The removal of the tSZ bias will allow cosmologicalinformation to be extracted from the CMB lensing cross-correlationsat much smaller angular scales than those used in DES Y1 analysis. This CMB lensing map will be useful for other cross-correlationsanalyses beyond those considered here.
- (2) A modeling framework built on the DES Y3 3 × 2pt correlations with CMB lensing.
- (3) A hybrid covariance matrix estimate for the 5 × 2pt data vector that combines three components: the 3 × 2pt halo-model covariance matrix from [83], an analytic log-normal covariance for the galaxy-CMB cross-covariance, and a model of the noise and mask contributions from realistic simulations.
- (4) A choice of angular scales to use when analyzing the CMB lensing cross-correlationsthat ensuresour cosmological constraints from data will be robust. even in the presenceof baryonic feedback and nonlinear galaxy bias. We describe two sets of

angular scale choicesone setthat is designed for the analysis that uses a linear galaxy bias model, and one designed for the analysis thatses a nonlinear galaxy bias model.

We use the methodological tools developed in this Here we reexamine the case for self-calibrating m using analysis to make forecasts for the cosmological constraints that will be obtained in our forthcoming analysis of actual the CMB lensing maps constructed here. The main results from these forecasts are

- (1) We forecast that our cross-correlation data vector will have a total signal-to-noise of 18.8 (20.8) when assuming linear(nonlinear) galaxy bias, which is about twice that obtained from past cross-correlation analyses between DES and SPT lensing using DES Y1 data [17].
- (2) When using the linear galaxy bias and the ΛCDM cosmology model, we expect to find a 3% constraint on S₈ using the cross-correlationdata vectors hδ_{KCMB}i b hγ_tκ_{CMB}i alone. ¹³ This constraint does not include any of the correlation functions that go into 3 × 2pt data vector analyzed in [15] and therefore serves as a powerful consistency test.
- (3) We anticipate a 2% constraint or from the 5 × 2pt analysis. Similar constraints are obtained when the nonlinear galaxy bias model is used.
- (4) When we do not apply external priors on the shear calibration parameters, we find that both 3 × 2pt and 5 × 2pt are able to calibrate the shear bias parameters, m, with 5 × 2pt roughly doubling the constraining power on these nuisance parameters. However, the resultant posteriors on the m parameters are still significantly weaker than the current external priors used by DES, suggesting that selfcalibration of shear biases from galaxy-CMB lensing cross-correlationis not likely to improve cosmological constraints in the near term. However, we emphasize that 5 × 2pt offers significantly tighter constraints than 3 × 2ptn the absence of external priors on shear calibration.

Cross-correlations of measurements of large-scale strucmethods presented in [57]. In particular, we describe from the Dark Energy Survey with measurements of our models for the galaxy and galaxy lensing cross-CMB lensing from the South Pole Telescope and Planck offer tight cosmological constraints that are particularly robust against sources of systematic error. Given the challenges of extracting unbiased cosmological constraints from increasingly precise measurements by galaxy surveys, we expectcross-correlations between galaxy surveys and CMB lensing to continue to play an important role in future cosmological analyses.

¹³We note that our analysis of ϸιδ_{CMB}i þ hγ_tκ_{CMB}i includes the so-called shear ratio likelihood, which acts as a prior on e.g., intrinsic alignments and the source redshiftstributions.

ACKNOWLEDGMENTS

National Science Foundation (NSF)through the Grant No. OPP-1852617. Partial support is also provided by the Kavli Institute of Cosmological Physics at the University of Chicago. Argonne National Laboratory's work was supported by the U.S.Department of Energy, Office of Science, Office of High Energy Physics, under Contract No. DE-AC02-06CH11357. Work at Fermi National AcceleratorLaboratory, a DOE-OS, HEP User Facility managed by the FermiResearch AllianceLLC, was supported under Contract No. DE-AC02-07CH11359 The Melbourne authors acknowledge supportfrom the Australian Research Council's Discovery Projects scheme (No. DP200101068). The McGill authors acknowledge funding from the Natural Sciences and Engineering Research Council of Canada, Canadian Institute for Advanced research and the Fonds de recherche du Quúbec Nature et technologies. The CU Boulder group acknowledges supporfrom NSF Grant No. AST-0956135. The Munich group acknowledges the support by the ORIGINS Cluster (funded by the Deutsche Forschungsgemeinschaft (DFG, German Research Foundation) under Germany's Excellence Strategy—EXC-2094-390783311), the Gesellschaft Faculty Fellowship Program, and the Ludwig-Maximilians-Universität München. J. V. acknowledges support from the Sloan Foundation. Funding for the 2013) including ERC Grant Agreements No. 240672, DES Projects has been provided by the U.S. Department of 291329, and No. 306478. We acknowledge support Energy, the U.S. National Science Foundation, the Ministry from the Brazilian Instituto Nacional de Ciência e of Science and Education of Spain, the Science and Technology Facilities Council of the United Kingdom, the Higher Education Funding Councilfor England, the National Center for Supercomputing Applications athe University of Illinois at Urbana-Champaignthe Kavli Institute of Cosmological Physics at the University of Chicago, the Center for Cosmology and Astro-Particle Physics at the Ohio State University, the Mitchell Institute for Fundamental Physics and Astronomy at Texas A&M University, Financiadora de Estudos e Projetos, Fundação Carlos Chagas Filho de Amparo `a Pesquisa do Estado do Rio de Janeiro, Conselho Nacional de Desenvolvimento Científico e Tecnológico and the Minisério da Ciência, Tecnologia e Inovação, the Deutsche Forschungsgemeinschaftd the Collaborating Institutions are Argonne National Laboratory, the University of California at Santa Cruz, the University of Cambridge, Centro de Investigaciones Energéticas, Medioambientales y Tecnológicas-Madrid, the University of Chicago, University College London, the DES-Brazil Consortium, the University of Edinburgh, the EidgenössischeTechnischeHochschule (ETH) Zürich, Fermi National Accelerator Laborator, the University of Illinois at Urbana-Champaignthe Institut de Cències de

l'Espai (IEEC/CSIC), the Institut de Física d'Altes The South Pole Telescope program is supported by the Ludwig-Maximilians Universität München and the associated Excellence Cluster Universe, the University of Michigan, NFS's NOIRLab, the University of Nottingham, The Ohio State University, the University of Pennsylvania, the University of Portsmouth, SLAC National Accelerator Laboratory, Stanford University, the University of Sussex, Texas A&M University, and the OzDES Membership Consortium. Based in part on observations at Cerro Tololo Inter-American Observatory at NSF's NOIRLab (NOIRLab Prop. ID 2012B-0001; PI: J. Frieman), which is managed by the Association of Universities for Research in Astronomy (AURA) under a cooperative agreement with the National Science Foundation. The DES data management ystem is supported by the National Science Foundation under Grants No. AST-1138766 and NoAST-1536171. The DES participants from Spanish institutions are partially supported by MICINN under Grants No. ESP2017-89838, No. PGC2018-094773No. PGC2018-102021No. SEV-2016-0588, No. SEV-2016-0597, and No. MDM-2015-0509, some of which include ERDF funds from the European Union. I. F. A. E. is partially funded by the CERCA program of the Generalitat de Catalunya. Research leading to these results has received funding from the European Research Council under the European Tecnologia (INCT) do e-Universo (CNPq Grant No. 465376/2014-2). This manuscripthas been authored by Fermi Research Alliance, LLC under Contract No. DE-AC02-07CH11359 with the U.S.Department of Energy.

> Note added in proof.—This work is part of a series of articles consisting of the analysis methodology (this paper), measurementson data [Chang et al. [102]] and the combined cosmological constraints [Abbott at. [103]].

APPENDIX A: CMB LENSING AUTOSPECTRUM

Office of Science, Office of High Energy Physics.

As a validation of our CMB lensing map, we also Institutions in the Dark Energy Survey. The Collaborating measure its auto-power spectrum and compare to previous measurementsThe raw CMB power spectrum contains noise bias terms which we must subtract off:

$$\hat{C}_{L}^{KK} \stackrel{1}{\cancel{4}} C_{L}^{\hat{K}\hat{K}} - N_{L}^{\delta0} - N_{L}^{\delta1}; \qquad \qquad \delta A1b$$

where the N^0Pand N^1Pterms are the noise terms from the disconnected and connected 4-functions [33]. In practice, we replace the $N_L^{\delta0b}$ term with the "realization

dependent" NO (RDN0) noise [104], which uses a mixture of simulation realizations and the data map itself:

where the subscripts fd: sq referto data and simulation realizations, φ_i represents the input lensing potential realization used to lens the CMB realization, and the superscriptx=SMICA denotes whetherwe are using the SPTb Planck or the SMICAnoSZ temperature mapsin this equation, we are representing the convergence maps used to compute the power spectrum inside the square brackets and the two temperature maps three used to reconstructhe lensing map with the round brackets.he different CMB realizations lensed with using a common lensing field:

where we highlight that the same CMB lensing potential is which gives us three lensing maps (a) TCMB only polynomials which gives us three lensing maps (a) TCMB only polynomials which gives us three lensing maps (a) TCMB only polynomials which gives us three lensing maps (a) TCMB only polynomials which gives us three lensing maps (b) the same CMB lensing potential is the same CMB lensing maps (b) the same CMB lensing potential is the same CMB lensing maps (b) the same CMB lensing potential is the same CMB lensing maps (b) the same CMB lensing maps (b) the same CMB lensing maps (b) the same CMB lensing maps (c) the same CMB lensing maps (b) the same CMB lensing maps (c) the same CMB lensing maps (d) the same CMB lensing map (d) the same CMB lensing ma debiased power spectrum is presented in Fig. 5. Compared to TCMB only to TCMB only to TCMB only to TCMB only to TCMBptSZ be the results of [20], we are able to extend our measurements to TCMB only to TCMBptSZ be the results of [20], we are able to extend our measurements to TCMBptSZ be the purpose of this demonstration, we improved treatment of point sources and clusters.

APPENDIX B: VALIDATING THE tSZ-NULLING METHOD

In this section, we verify that the methodology describe dudes against the unbiased case (i.e., taking the ratios in Sec. II D 2 results in a tSZ bias free CMB lensing map using a simplified two-componen(CMB and tSZ) simulation. This is demonstrated in two steps:

- (1) We first show that SMICAnoSZ is free of the tSZ effect.
- (2) We perform lensing reconstruction with one temperature map free of tSZ effect, and demonstrate that the reconstructed lensing map is free oftSZ

tSZ maps at 100-857 GHz generated from an N-body

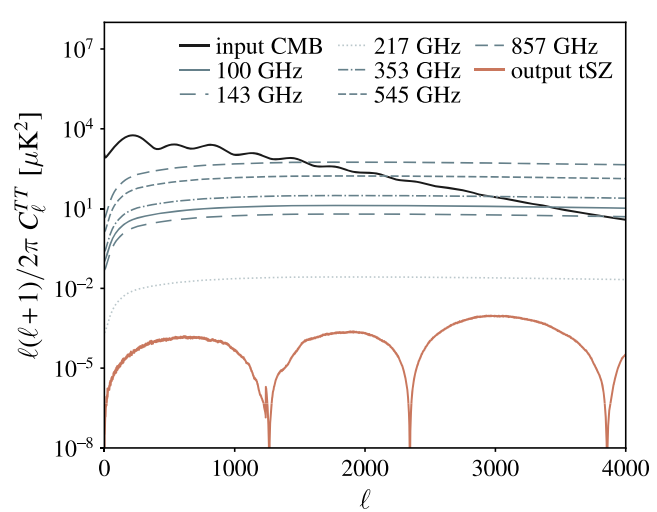


FIG. 16. tSZ power spectra at 100=143=217=353=545= 857 GHz (various blue lines), as well as the tSZ residual power spectrum after passing the individual frequency maps through the SMICAnoSZ weights (orange).

simulation [40], and multiply each frequency channel N_I^{ŏ1b}bias term can be computed using simulated maps witthith the weights given by the SMICA weight propagation code.14 The power spectra of the tSZ effect at 100=143=217=353=545=857 GHz channels and the resulting spectra after passing through the weights are shown in Fig. 16. We find that the resulting tSZ amplitude is suppressed to negligible levels as expected.

> Next, we construct a lensing map from the combination of two types of temperature maps

- (1) CMB only maps to mimic tSZ nulled CMB maps (i.e., Planck SMICAnoSZ map) and
- (2) CMB b tSZ maps to mimic high resolution CMB

higher multipoles because of the nulling of the tSZ bias and sume f_{ky} 1, and add noise that is reduced by a factor of 100 to reduce the computational cost of averaging over many realizations. We carry out the lensing reconstruction procedure, measure the cross-correlation sbetween the reconstructed lensing maps and a mock galaxy density map, and compare the resulting cross-correlation ampli-

> ððbÞ-ðaÞÞ=ðaÞ and ððcÞ-ðaÞÞ=ðaÞÞ. The results are shown Fig. 17: we observe that the lensing map without any treatment of the tSZ effect is biased low, whereasthe lensing map produced using the "half-leg" method is compatible with the lensing map produced from "CMB only" temperature maps.

¹⁴COM_Code_SMICAweightspropagation_R3.00 available from Planck Legacy Archieve https://pla.esac.esa.int/. For the first step, we take a lensed CMB map and simulated specifically use the values from weights_T_smicanosz R3.00 Xfull.txt.

ay ofsampling the uncern-a framework referred e, HYPERRANK is more ertainty in photometric tion in the entire shape of the nelis typically broad, the izing the mean redshift 2] it is shown that the sing HYPERRANK are ng the mean redshift, which re and in [15], which is to sample. However, in [15] hown that when applied esults in cosmological the fiducial analysis by all constraints. We compare aints using the fiducial nðzÞ with shiftparameter, int improvementin the $\Omega_m = \sigma_8 = S_8$ went from

(orange).

CALE CUTS FOR BIAS MODEL

n using the nonlinear galaxy he same framework of

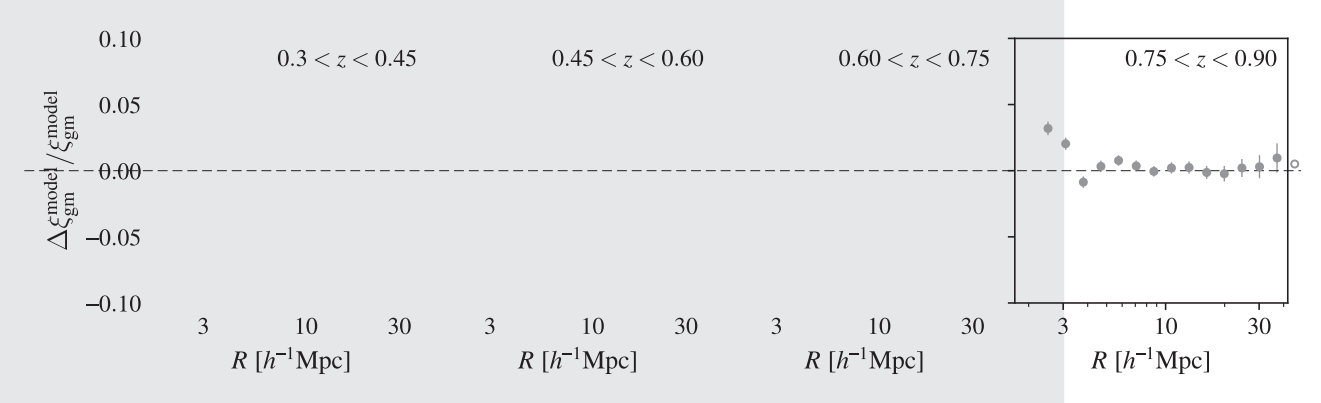


FIG. 18. Residuals of best-fißD galaxy-matter correlation function in the MICE simulation (with the MGLIM galaxy sample) assuming a nonlinear galaxy bias model. The shaded region indicates bias exceeding 3%, which we exclude in our analysis when we assume nonlinear galaxy bias.

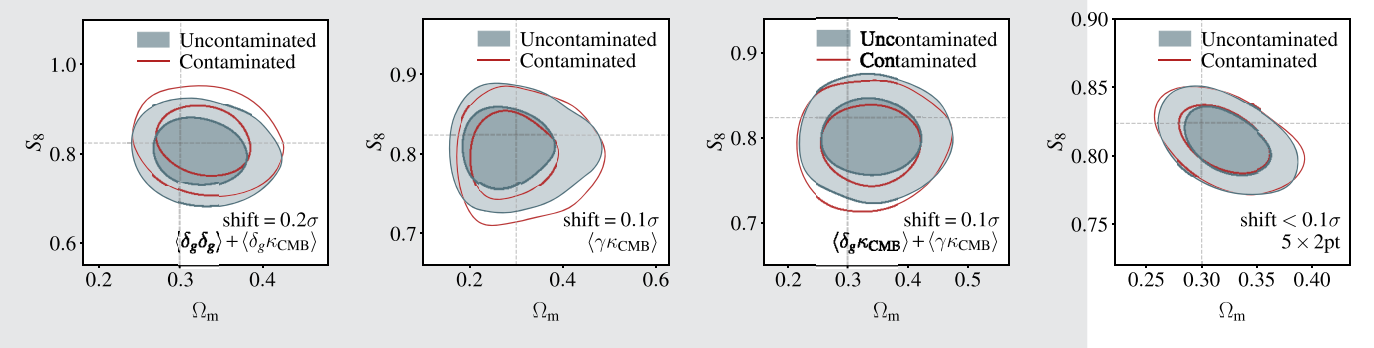


FIG. 19. Same as Fig.12 but for the REDMAGIC sample.

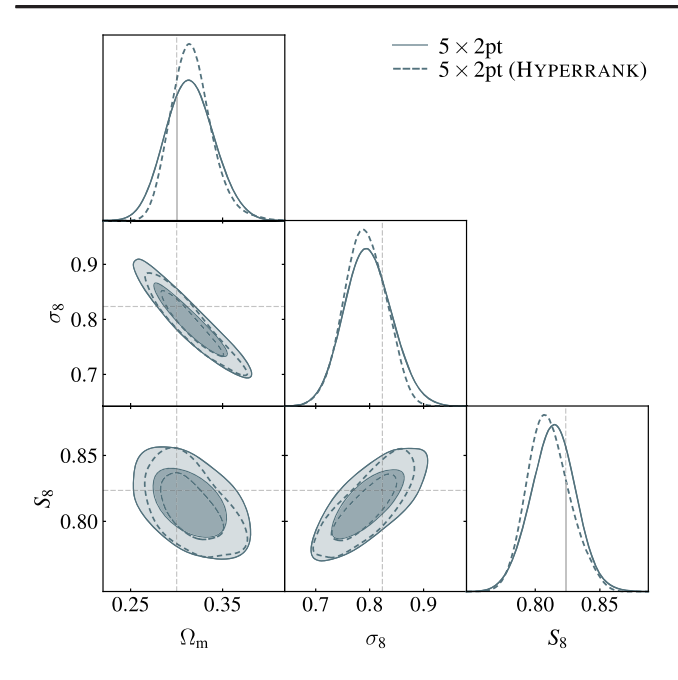


FIG. 20. Comparison of the forecasted constraints, once-S₈ plane when using the fiducial model of assuming a shift in not scale cut choice is still relatively conservative. and when drawing from possible realizations using HYPERRANK.

choosing scale cuts for haccomb since the contaminated data vector thatwe use to perform the testis generated using our nonlinear bias model. Instead, we need an

a priori criteria for where the PT-based nonlinear galaxy bias model fails to describe the galaxy-matter power spectrum. We take an approach similar to that used in [105] where we measure the 3D galaxy-matter correlation function from a set of N-body simulations, namely the MICE simulations [95,96]. These simulations include mock galaxies that have similar selection functions as our lens galaxies (i.e. the MGLIM and REDMAGIC samples). We fit the measurements using the nonlinear bias model described in Eq.(13) and the input cosmological parameters to the simulations. Figure 18 shows the relative residuals of the fit for the four tomographic lens bins for the MagLim sample.

Based on Fig.18, we decide to include scales down to ~3 Mpc/h. This gives at most 3% difference between model and simulation data, compared to the statistical error bars in hδ_{κ_{CMB}} at about 10%. We note that out of the 50 or so data points, only 2 are above 1%. In addition, in the real cosmological analysis, there will be many more degrees of freedom in the other nuisance parameters (IA, photo-z etc.), which will further absorb this bias. These factors suggest that

APPENDIX E: REDMAGIC

In this section, we summarize the parameter ranges used in the analysis (Table V), scale cut used (Table VI),

TABLE V. Same as the lens galaxy section of Table III but for the REDMAGIC sample.

Parameter	Prior	Fiducial		
REDMAGIC				
b ¹⁵	U½0.8; 3.0	1.7, 1.7, 1.7, 2.0, 2.0		
b ₁ ¹⁵	U½0.67; 3.00	1.40, 1.40, 1.40, 1.40, 1.65, 1.65		
b ₂ ¹⁵	U1⁄₂−4.22; 4.22	0.16, 0.16, 0.16, 0.35, 0.35,		
C ₁ 5	Fixed	1.31, -0.52, 0.34, 2.25, 1.97		
$\Delta_{7}^{15} \times 10^{-2}$	N ½0.0; 0.4N ½0.0; 0.3N ½0.0; 0.3N ½0.0; 0.5N ½0.0; 1.0	0.0, 0.0, 0.0, 0.0, 0.0		
σ _z ¹⁵	Fixed, fixed, fixed, fixed N 1/21.0; 0.054	1.0, 1.0, 1.0, 1.0, 1.0		

TABLE VI. Same as Table IV but for the EDMAGIC sample.

Туре	Redshiftbin	$ heta_{min}$		Forecasted S=N		
		SPTþPlanck	Planck	SPTþPlanck	Planck	Combined
hδ _g κ _{CMB} i	1	15.8 (11.8)	13.8 (11.8)			
	2	11.7º (8.8º)	10.2º (8.8º)			
	3	10.0° (7.5°)	8.7º (7.5º)			
	4	9.00 (6.89)	7.9º (6.8º)			
	5	8.6º (6.4º)	7.5º (6.4º)			
	All bins	, ,	,	11.1 (13.0)	10.9 (11.7)	15.6 (17.5)
hγκ _{CMB} i	1	2.5°	2.5°	,	, ,	,
i. OMB	2	2.5°	2.5°			
	3	11.2 ⁰	2.5°			
	4	17.7 ⁰	2.5°			
	All bins			10.1	8.7	13.3
hδκ _{CMB} i þ hγ _t κ _{CMB} i	All bins			13.2 (14.5)	12.2 (12.8)	18.0 (19.4)

forecasted signal-to-noise ratio (Table VI) as well as figur**sa**mple. We find that scale cuts similar to that of the for the parametercontour shifts (Fig. 19), equivalent o MAGLIM sample allow us to pass our bias requirements, Tables III and IV and Fig. 12 respectively, when using the and we forecast that the signal-to-noise ratio will be marginally lower for the REDMAGIC sample.

- [1] The Dark Energy Survey Collaboration arXiv:astro-ph/ 0510346.
- [2] J. T. A. de Jong, K. Kuijken, D. Applegate et al., The Messenger 15444 (2013).
- [3] H. Aihara, N. Arimoto, R. Armstrong et al., Publ. Astron. Soc.Jpn.70, S4 (2018).
- [4] T. Giannantonio, P. Fosalba, R. Cawthon et al., Mon. Not. R. Astron. Soc. 456, 3213 (2016).
- [5] Y. Omori, T. Giannantonio, A. Porredon et al., Phys. Rev. D 100, 043501 (2019).
- [6] Y. Omori, E. J. Baxter, C. Chang et al., Phys. Rev. D 100, 043517 (2019).
- [7] T. Namikawa, Y. Chinone, H. Miyatake et al., Astrophys. J. 882, 62 (2019).
- [8] A. Krolewski, S. Ferraro, E. F. Schlafly, and M. White, J. Cosmol.Astropart.Phys.05 (2020) 047.
- [9] O. Darwish, M. S. Madhavacheril, D. Sherwin et al., Mon. Not. R. Astron. Soc. 500, 2250 (2021).
- [10] N. C. Robertson, D. Alonso, J. Harnois-Déraps et al., Astron. Astrophys. 649, A146 (2021).
- [11] M. White, R. Zhou, J. DeRose et al., J. Cosmol. Astropart. Phys.02 (2022) 007.
- [12] E. Baxter, J. Clampitt, T. Giannantonio et al., Mon. Not. R. Astron. Soc. 461, 4099 (2016).
- [13] E. Schaan, E. Krause, T. Eifler, O. Doré, H. Miyatake, J. Rhodes, and D. N. Spergel, Phys. Rev. D 95, 123512 (2017).
- [14] J. E. Carlstrom, P. A. R. Ade, K. A. Aird et al., Publ. Astron. Soc. Pac. 123, 568 (2011).
- [15] DES CollaborationPhys.Rev.D 105, 023520 (2022)
- [16] N. Aghanim, Y. Akrami et al. (Planck Collaboration), Astron. Astrophys.641, A8 (2020).
- [17] DES & SPT Collaborations, Phys. Rev. D 100, 023541 (2019).
- [18] E. J.Baxter, Y. Omori, C.Chang et al., PhysRev. D 99, 023508 (2019).
- [19] K. T. Story, C. L. Reichardt, Z. Hou et al., Astrophys. J. 779, 86 (2013).
- [20] Y. Omori, R. Chown, G. Simard et al., Astrophys. J. 849, 124 (2017).
- [21] R. Chown, Y. Omori, K. Aylor et al., Astrophys. J. Suppl. Ser.239, 10 (2018).
- [22] L. E. Bleem, B. Stalder, T. de Haan etal., Astrophys. J. Suppl. Ser. 216, 27 (2015).
- [23] J. A. Tauber, N. Mandolesi, J. L. Puget et al., Astron. Astrophys. 520, A1 (2010).
- [24] Planck Collaboration, Astron. Astrophys. 536, A1 (2011).
- [25] N. Aghanim, Y. Akrami et al. (Planck Collaboration), Astron. Astrophys.641, A3 (2020).

- [26] T. Okamoto and W. Hu, Phys. Rev. D 67, 083002 (2003).
- [27] J. Delabrouille, J. F. Cardoso, and G. Patanchon, Mon. Not. R. Astron. Soc. 346, 1089 (2003).
- [28] J.-F. Cardoso, M. Le Jeune, J. Delabrouille et al., IEEE J. Sel. Top. Signal Process2, 735 (2008).
- [29] Y. Akrami, M. Ashdown et al. (Planck Collaboration), Astron. Astrophys. 641, A4 (2020).
- [30] J. Bobin, F. Sureau, and J. L. Starck, Astron. Astrophys. 591, A50 (2016).
- [31] M. S. Madhavacheril, J. C. Hill, S. Næss et al., Phys. Rev. D 102, 023534 (2020).
- [32] L. E. Bleem, T. M. Crawford, B. Ansarinejad etal., Astrophys. J. Suppl. Ser. 258, 36 (2022).
- [33] P. A. R.Ade, N. Aghanim et al. (Planck Collaboration), Astron. Astrophys. 571, A17 (2014).
- [34] P. A. R.Ade, N. Aghanim et al. (Planck Collaboration), Astron. Astrophys. 594, A15 (2016).
- [35] N. Aghanim, Y. Akrami et al. (Planck Collaboration), Astron. Astrophys. 641, A6 (2020).
- [36] A. Lewis, LensPix: Fast MPI full sky transforms for HEALPix (2011), ascl:1102.025.
- [37] E. M. George, C. L. Reichardt, K. A. Aird et al., Astrophys. J. 799, 177 (2015).
- [38] W. B. Everett, L. Zhang, T. M. Crawford et al., Astrophys. J. 900, 55 (2020).
- [39] S. Ferraro and J. C. Hill, Phys. Rev. D 97, 023512 (2018).
- [40] Y. Omori, arXiv:2212.07420.
- [41] N. Sehgal, P. Bode, S. Das, C. Hernandez-Monteagudo, K. Huffenberger, Y.-T. Lin, J. P.Ostriker, and H. Trac, Astrophys. J. 709, 920 (2010).
- [42] D. Lenz, O. Doé, and G. Lagache, Astrophys. J. 883, 75 (2019).
- [43] T. M. Crawford, R. Chown, G. P. Holder et al., Astrophys. J. Suppl. Ser. 227, 23 (2016).
- [44] Y. Hoffman and E. Ribak, Astrophys. J. Lett. 380, L5 (1991).
- [45] A. Benoit-Lévy, T. Déchelette, K. Benabed, J. -F. Cardoso, D. Hanson, and S. Prunet, Astron. Astrophys. 555, A37 (2013).
- [46] M. S. Madhavacheriland J. C. Hill, Phys. Rev. D 98, 023534 (2018).
- [47] S. J. Osborne, D. Hanson, and O. Doré, J. Cosmol. Astropart. Phys. 03 (2014) 024.
- [48] E. Schaan and SFerraro, Phys. Rev. Lett. 122, 181301 (2019).
- [49] E. J.Baxter, R. Keisler, S. Dodelson et al., Astrophys. J. 806, 247 (2015).
- [50] A. van Engelen, S. Bhattacharya, N. Sehgal, G. P. Holder,O. Zahn, and D. Nagai, Astrophys. J. 786, 13 (2014).

- [51] G. P. Holder, M. P. Viero, O. Zahn et al., Astrophys. J. Let [81] G. Giannini et al. (to be published). 771, L16 (2013).
- [52] P. A. R.Ade, N. Aghanim et al. (Planck Collaboration), Astron. Astrophys. 571, A18 (2014).
- [53] A. van Engelen, B. D. Sherwin, N. Sehgalet al., Astrophys.J. 808, 7 (2015).
- [54] A. S. Maniyar, M. Béthermin, and G. Lagache, Astron. Astrophys.614, A39 (2018).
- [55] Y. Cao, Y. Gong, C. Feng, A. Cooray, G. Cheng, and X. Chen, Astrophys. J. 901, 34 (2020).
- [56] W. L. K. Wu, L. M. Mocanu, P. A. R. Ade et al., Astrophys.J. 884, 70 (2019).
- [57] E. Krause etal. (to be published).
- [58] A. Porredon et al. (DES Collaboration), Phys. Rev. D 103 043503 (2021).
- [59] E. S.Rykoff, E. Rozo, M. T. Busha etal., Astrophys.J. 785, 104 (2014).
- [60] E. S. Rykoff, E. Rozo, D. Hollowood et al., Astrophys. J. Suppl. Ser. 224, 1 (2016).
- [61] S. Pandey etal., arXiv:2105.13545.
- R. Astron. Soc. 504, 4312 (2021).
- [63] J. Myles, A. Alarcon et al. (DES Collaboration), Mon. Not. R. Astron. Soc. 505, 4249 (2021).
- [64] D. N. Limber, Astrophys. J. 117, 134 (1953).
- [65] A. Lewis, A. Challinor, and A. Lasenby, Astrophys. J. 538, 473 (2000).
- [66] R. Takahashi, M. Sato, T. Nishimichi, A. Taruya, and M. Oguri, Astrophys.J. 761, 152 (2012).
- [67] A. J. Benson, S. Cole, C. S. Frenk, C. M. Baugh, and C. G. Lacey, Mon. Not. R. Astron. Soc. 311, 793 (2000)
- [68] P. McDonald and A. Roy, J. Cosmol. Astropart. Phys. 08 (2009)020.
- [69] S. Saito, T. Baldauf, Z. Vlah, U. Seljak, T. Okumura, and P. McDonald, Phys. Rev. D 90, 123522 (2014).
- [70] S. Pandey, E. Krause, J. DeRose et al., Phys. Rev. D 106, 043520 (2022).
- [71] X. Fang, J. A. Blazek, J. E. McEwen, and C. M. Hirata, J. [97] A. Amon et al., Phys.Rev.D 105, 023514 (2022). Cosmol.Astropart.Phys.02 (2017) 030.
- [72] M. Bartelmann and P.Schneider, Phys. Rep. 340, 291 (2001).
- [73] J. Verner VillumsenarXiv:astro-ph/9512001.
- [74] R. Moessner and B. Jain, Mon. Not. R. Astron. Soc. 294, [100] A. Vallinotto, Astrophys. J. 759, 32 (2012). L18 (1998).
- [75] F. Schmidt, E. Rozo, S. Dodelson, L. Hui, and E. Sheldon, Phys.Rev.Lett. 103, 051301 (2009).
- [76] J. Elvin-Poole, N. MacCrann et al. (to be published).
- [77] C. M. Hirata and U. Seljak, Phys. Rev. D 70, 063526 (200,40,3] T. M. C. Abbott et al., this issue, Phys. Rev. D 107, 023531
- [78] S. Bridle and L. King, New J. Phys. 9, 444 (2007).
- [79] J. A. Blazek, N. MacCrann, M. A. Troxel, and X. Fang, Phys.Rev.D 100, 103506 (2019).
- [80] R. Cawthon et al. (DES Collaboration), Mon. Not. R. Astron. Soc. 513, 5517 (2022).

- [82] J. P. Cordero, I. Harrison et al., Mon. Not. R. Astron. Soc. 511, 2170 (2022).
- [83] O. Friedrich et al. (DES Collaboration), Mon. Not. R. Astron. Soc. 508, 3125 (2021).
- [84] S. Hilbert, J. Hartlap, and P. Schneider, Astron. Astrophys. 536, A85 (2011).
- [85] O. Friedrich, D. Gruen, J. DeRose et Alhys. Rev. D 98, 023508 (2018).
- [86] R. Mandelbaum, C. M. Hirata, A. Leauthaud, R. J. Massey, and J. Rhodes, Mon. Not. R. Astron. Soc. 420, 1518 (2012).
- [87] E. van Uitert, B. Joachimi, S. Joudaki et al., Mon. Not. R. Astron. Soc. 476, 4662 (2018).
- [88] N. MacCrann, J. Blazek, B. Jain, and E. Krause, Mon. Not. R. Astron. Soc. 491, 5498 (2020).
- [89] H. S. Xavier, F. B. Abdalla, and B. Joachimi, Mon. Not. R. Astron. Soc. 459, 3693 (2016).
- [90] C. Sánchez, J. Prat et al., Phys. Rev. D 105, 083529 (2022)
- [62] M. Gatti, E. Sheldon et al. (DES Collaboration), Mon. Not. [91] N. E. Chisari, M. L. A. Richardson, J. Devriendt, Y. Dubois, A. Schneider, A. M. C. Le Brun, R. S. Beckmann, S. Peirani, A. Slyz, and C. Pichon, Mon. Not. R. Astron. Soc. 480, 3962 (2018).
 - [92] H.-J. Huang, T. Eifler, R. Mandelbaum, and S. Dodelson, Mon. Not. R. Astron. Soc. 488, 1652 (2019).
 - [93] V. Desjacques, D. Jeong, and F. Schmidt, Phys. Rep. 733, 1 (2018).
 - [94] J. Schaye, C. Dalla Vecchia, C. M. Booth, R. P. C. Wiersma, T. Theuns, M. R. Haas, S. Bertone, A. R. Duffy, I. G. McCarthy, and F. van de Voort, Mon. Not. R. Astron. Soc. 402, 1536 (2010).
 - [95] P. Fosalba, M. Crocce, E. Gaztañaga, and F. J. Castander, Mon. Not. R. Astron. Soc. 448, 2987 (2015).
 - [96] M. Crocce, F. J. Castander, E. Gaztañaga, P. Fosalba, and J. Carretero, Mon. Not. R. Astron. Soc. 453, 1513 (2015).
 - - [98] L. F. Secco, S. Samuroff et al. (DES Collaboration), Phys. Rev.D 105, 023515 (2022).
 - [99] C. Hirata and U.Seljak, Mon. Not. R. Astron. Soc. 343, 459 (2003).

 - [101] N. MacCrann etal. (DES Collaboration), Mon. Not. R. Astron. Soc. 509, 3371 (2022).
 - [102] C. Chang et al., following paper, Phys. Rev. D 107, 023530 (2023).
 - (2023).
 - [104] T. Namikawa, D. Yamauchi, and A. Taruya, J. Cosmol. Astropart. Phys. 01 (2012) 007.
 - [105] S. Pandey, E. Krause, B. Jain et al., Phys. Rev. D 102, 123522 (2020).